Finite Tube Method for buckling analysis of tubular members using Fourier-approximation for the displacements

Sándor Ádány[1], Benjamin W. Schafer[2]

Abstract

In this paper an efficient numerical method for the static analysis of cylindrical tubes is introduced. The method is designed for the linear buckling analysis of wind turbine support towers which are, most typically, built up from conical and/or cylindrical cans. Accordingly, the developed method uses cylindrical tube segments as elementary building blocks, along with specialized shape functions, and is named the Finite Tube Method. Within a tube segment the displacements are approximated by two-dimensional Fourier series. The curved nature of the surface is directly considered in the kinematic equations. The segments are joined and/or supported to the ground by constraint equations or by elastic links. In the current implementation internal stresses are determined in a simplified way: the circumferential stress distributions are calculated from the internal forces/moment by classic strength of material formulae, while the longitudinal distribution within each segment is quadratic. The considered internal forces/moments are: normal force, shear force, bending moment, and torsional moment. The internal forces can be arbitrarily combined. In the paper the underlying derivations are briefly summarized, then the method is demonstrated and validated by numerical examples, comparing the results to analytical and alternative numerical solutions. The authors are actively developing the method and will provide future work on utilization of the method for buckling mode identification and decomposition, as well as practical advancements to make the method a useful tool in the engineering design and analysis of wind turbine support towers.

Keywords

tubular members, linear buckling analysis, Finite Tube Method

1. Introduction, motivation

Tubular members or cylindrical shells are found in many fields of engineering. They can be large (e.g., silos), or smaller-size (e.g., bars in truss structures), or even microscopic size (e.g., nano-tubes). Nowadays, they are extensively used as supporting structures of wind turbines, dictated by the need for producing sustainable electricity. Wind turbine towers are simple cantilevers, but subjected to a combination of various load components, including normal force (N), bending moment (M), shear force (V) and torsion (T). Since they are slender, they are potentially subjected

[1]Associate Research Scientist, Johns Hopkins University, asandor2@jhu.edu
Professor, Budapest University of Technology and Economics, adany.sandor@emk.bme.hu
[2] Professor, Johns Hopkins University, schafer@jhu.edu

to instability. In fact, buckling (along with fatigue) is one of the major aspects that governs the structural design [1].

A classic way to evaluate stability problems is to assume a perfectly elastic and imperfection-free structure, but to consider the quadratic (i.e., nonlinear) terms in the kinematic equations, which results in a linear buckling analysis (LBA), or, elastic buckling analysis. Mathematically, LBA is a generalized eigen-value problem. In structural stability problems the eigenvalues are the critical load factors, and the eigenvectors are the specific displacement vectors, i.e., buckled shapes. Though stability phenomena are influenced by imperfections, LBA is still involved in many design procedures as it provides a robust and reproducible parameter for assessing stability. Though shell structures are known to be particularly sensitive to (geometric) imperfections, elastic buckling remains a useful tool. LBA is a prominent way to understand the basic stability phenomena as well as the imperfection sensitivity in thin shells [2]. Moreover, the calculation of the slenderness parameters, required by design standards [1], is directly dependent on the critical stress values.

Elastic buckling problems of cylindrical shells have been discussed in a large number of papers during the last century, hence, a comprehensive overview of the relevant papers is impossible. It can be concluded that analytical solutions for shell-type buckling of tubular members are limited only to simple cases, (i.e., members with simple supports subjected to simple loading such as pure compression or pure bending,) which are summarized in classic textbooks [e.g., 3-5]. Approximate solutions/formulae for specific buckling types are also available, e.g., in design codes [1].

Nowadays, obviously, numerical solutions are easily available, mostly by the finite element method (FEM) using shell finite elements. However, it is worth noting that shell FEM buckling solutions for tubes require a fine discretization [6], and can lead to a large number of shell finite elements and degrees of freedom, especially if the analyzed member is long. Thus, shell FEM is computationally expensive, and can be demanding even with today's computers. There is still ongoing research efforts to develop computationally efficient numerical methods for shells, see e.g., [7-8].

An alternative to shell FEM for the analysis of general thin-walled members is the Generalized Beam Theory. This was first employed to circular tubes by Silvestre [9], where the (so-called) conventional deformation modes were derived and applied. To make the method more general and more accurate, further modes were considered in [10-11]. Recently, the method was further generalized, e.g., by considering conical tubes [12], or, circular tubes with curved axis [13-14]. The latest related development is by Nedelcu, who proposed novel GBT deformation modes, specifically developed for circular tubes [15-16] and discussed further herein.

Another popular alternative to shell FEM for the analysis of general thin-walled members is the Finite Strip Method [17-18]. Its most important feature (and difference compared to shell FEM) is that the displacements are approximated partly by trigonometric functions. The practical advantage of FSM is that it is very efficient computationally for certain, relatively simple but typical problems. However, FSM implementation for circular tubes is not known.

In this paper a newly developed numerical analysis tool is introduced, which essentially follows the logic of FSM. The method is designed to be a compromise between analytical solutions and general shell FEM solutions: with much more general applicability than that of the available analytical formulae, but with more numerical efficiency and customizability than a shell FEM calculation. The method uses Fourier-series approximation for the displacements both in the circumferential and longitudinal directions. In the strain-displacement relationship the circumferentially curved geometry is directly considered.

The Fourier-series displacement approximation does not require traditional discretization. However, wind turbine towers are globally tapered. Global tapering can be achieved by fabrication of conical cans/segments which are joined by welded and/or bolted connections. Alternatively, towers can be built up from cylindrical cans/segments, with the diameter and thickness of the them varying along the length, leading to a slight taper in the towers [19]. Therefore, the developed method – optionally – uses discretization along the member length, which enables the consideration of small cross-section changes, and makes it possible to more accurately approximate any longitudinal variation in the internal actions, which again, is typical for wind turbine towers. The elementary building block of the developed method is a tubular segment, and the structural model is built up from these segments, the method will be termed here as the Finite Tube Method, abbreviated as FTM, following the naming logic of the Finite Element Method (FEM), Finite Strip Method (FSM), Finite Prism Method (FPM), etc.

As it turns out, during the work reported here, related research has been completed by Nedelcu, as in [15-16]. The applied mechanical assumptions and displacement functions in [16] and in the method reported here are quite similar. Still, there are important differences, which will further be discussed in the paper, as follows: (a) Nedelcu follows the GBT methodology in developing his method, while we use a methodology more similar to FSM/FEM, (b) there are some differences in the applied geometric equations, (c) we apply longitudinal discretization by joining the tubular segments, enabling the approximate calculation of non-uniform tubular members.

Though developing an efficient analysis tool is useful in itself, the goal of the authors is to incorporate into the tube buckling problem the knowledge and techniques used in other fields of structural stability. However, all these further developments are out of the limits of this paper, which is foundational, summarizing the basics of the newly developed FTM. In Section 2 the method is described. Section 3 presents numerical examples, partly to validate the developed method, and partly to show its potential. In Section 4, before Conclusions, some aspects of the method are further discussed.

2. Summary of the FTM

2.1 The displacements for a segment

The studied tubular segment is geometrically defined by its radius, R, thickness, t, and length, L, where the radius is interpreted as the mean of the radii of the outer and inner surfaces, see Fig. 1. For the description of the displacements we introduce a local coordinate system. Three displacement functions are involved, u, v, and w, where v is longitudinal, i.e., in the y-direction, and u and w are transverse displacements: u being circumferential translation, and w being radial translation (in the x- and z-direction, respectively). Note, that x is a circumferential coordinate, i.e., the local x-axis is curved.

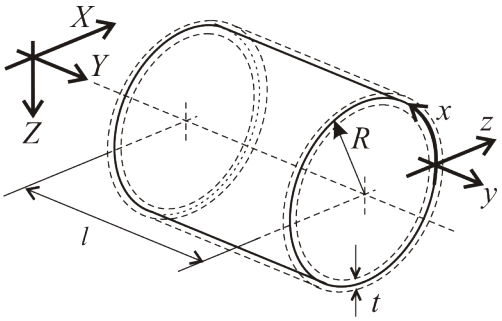

Figure 1: A tube segment, with basic notations

The displacement functions are approximated identically, by Fourier series. The u, v, and w translations are expressed as:

$$u(x,y) = \sum_{k=1}^{n} u_k f_k(x,y) \quad v(x,y) = \sum_{k=1}^{n} v_k f_k(x,y) \quad w(x,y) = \sum_{k=1}^{n} w_k f_k(x,y) \tag{1}$$

where n is the total number of terms. The $f(x,y)$ functions are (mostly) trigonometric functions, as detailed in Appendix A. Two possible sets of basis functions are presented in Appendix A; they are identical in the circumferential direction, but different in the longitudinal direction. Two Fourier-like series are considered in the longitudinal direction (i) classic Fourier-series with sin and cos terms (denoted 'sin-cos' version), and (ii) augmented sin series where only sin terms are applied, but supplemented by a linear term as well (denoted 'sin-only' version). Section 4 provides additional discussion on accuracy and efficiency of the two versions.

2.2 The strains

From the displacements the strains are calculated by directly considering the curved nature of the geometry. In particular, strains are similar to those in [9] or [16], which are based on Sanders shell theory [20]. To calculate the strains, first, the slopes (β) of the displacement functions (i.e., angles to the x-, y-, and z-axis) are defined as the surface is displaced:

$$\beta_x = -\frac{\partial w}{\partial y} \quad \beta_y = \frac{u}{R} - \frac{\partial w}{\partial x} \quad \beta_z = -\frac{\partial u}{\partial y} \tag{2}$$

From the slopes the curvatures (κ) are:

$$\kappa_{xx} = \frac{\partial \beta_y}{\partial x} \quad \kappa_{yy} = \frac{\partial \beta_x}{\partial y} \quad \kappa_{xy} = \frac{\partial \beta_x}{\partial x} + \frac{\partial \beta_y}{\partial y} + \frac{\beta_z}{R} \tag{3}$$

The linear strain components are as follows:

$$\varepsilon_x{}^L = \frac{\partial u}{\partial x} + \frac{w}{R} + z\,\kappa_{xx} \quad \varepsilon_y{}^L = \frac{\partial v}{\partial y} + z\,\kappa_{yy} \quad \gamma_{xy}{}^L = \frac{\partial v}{\partial x} + \frac{\partial u}{\partial y} + z\,\kappa_{xy} \tag{4}$$

The nonlinear components are as follows:

$$\varepsilon_x{}^{NL} = 0 \quad \varepsilon_y{}^{NL} = \frac{1}{2}\left(\beta_x{}^2 + \left(\frac{\partial v}{\partial y}\right)^2 + \beta_z{}^2\right) \quad \gamma_{xy}{}^{NL} = \left(\frac{\partial u}{\partial x} + \frac{w}{R}\right)\frac{\partial u}{\partial y} + \frac{\partial v}{\partial x}\frac{\partial v}{\partial y} + \beta_x\beta_y \tag{5}$$

The second-order (nonlinear) hoop strains are disregarded in this paper, but can be added later. Note, as the curvature of the surface vanishes (and therefore R tends to infinity), the expressions for the strains become identical to those based on the Green-Lagrange strain tensor of a general flat plate+membrane theory. Utilizing the expressions in this form leads to minor differences from [9] and [16], but aligns the method with well-known numerical methods for thin-walled structural members [17-18], as well as classic thin shell finite elements e.g., [21]. Additional discussion regarding the impact of the selected kinematics is provided in Section 4.

2.3 The stresses and stress resultants

In a typical finite element buckling solution the internal stresses (which are necessary to determine the tangent stiffness of the structure) are calculated by a linear static analysis. Though this path could readily be followed here, for the sake of simplicity, the internal stresses are taken here without performing a formal linear static analysis. Hence, similarly to the finite strip method, see [17], we assume the internal stresses and connect them directly to section-level actions, as opposed to common numerical stability analysis where loads are applied and these are used to find the internal stresses.

The *x*-direction (hoop) normal stresses are disregarded. For the other two components, in the longitudinal direction the distribution is assumed to be quadratic (or, as a particular case, either linearly varying or uniform). In the circumferential direction the distributions of the stresses are assumed to be either constant or sinusoidal, to generate 4 pure loading cases: pure N, pure M, pure T, and pure V. The 4 loading cases can arbitrarily be combined. The stress functions, in mathematical form, and how the stresses are related to the stress resultants are given in Appendix B.

It is to note that the pure V case is unique, though theoretically possible it is hard to imagine V without moment gradient; however, it is still useful to isolate and understand its effect on the buckling behavior and a similar approach was followed by [22] when investigating the effect of shear in cold-formed steel members.

2.4 Total potential

Isotropic, linear elastic material is considered. The internal part of the total potential is, therefore:

$$\Pi_{int} = \frac{1}{2}\int_0^L \int_0^{2R\pi} \int_{-t/2}^{+t/2} \boldsymbol{\varepsilon_L}^{\mathrm{T}} \mathbf{D} \boldsymbol{\varepsilon_L} \mathrm{d}x\mathrm{d}y\mathrm{d}z \tag{6}$$

where

$$\mathbf{D} = \begin{bmatrix} E & \nu E & 0 \\ \nu E & E & 0 \\ 0 & 0 & G \end{bmatrix} \tag{7}$$

$$\boldsymbol{\varepsilon_L}^{\mathrm{T}} = \begin{bmatrix} {\varepsilon_x}^L & {\varepsilon_y}^L & {\gamma_{xy}}^L \end{bmatrix} \tag{8}$$

and E and G are the Young's and shear modulus, respectively, and ν is the Poisson's ratio.

The external part of the total potential is calculated from the stresses and the nonlinear strains, as:

$$\Pi_{ext} = -t\int_0^L \int_0^{2R\pi} \boldsymbol{\varepsilon_{NL}}^{\mathrm{T}} \boldsymbol{\sigma} \mathrm{d}x\mathrm{d}y \tag{9}$$

where

$$\boldsymbol{\varepsilon_{NL}}^{\mathrm{T}} = \begin{bmatrix} {\varepsilon_x}^{NL} & {\varepsilon_y}^{NL} & {\gamma_{xy}}^{NL} \end{bmatrix} \tag{10}$$

$$\boldsymbol{\sigma}^{\mathrm{T}} = \begin{bmatrix} \sigma_x & \sigma_y & \tau_{xy} \end{bmatrix} \tag{11}$$

2.5 Stiffness matrices for a single segment

By using the theorem of stationarity of the potential energy, we need to take the partial derivatives of the potential energy function with respect to the Fourier coefficients, which leads to a system of n linear equations. The equation system is homogeneous, and it reads – for the m-th segment – as follows:

$$\left(\mathbf{k}_{\mathbf{e}[\mathbf{m}]} - \lambda \mathbf{k}_{\mathbf{g}[\mathbf{m}]}\right)\mathbf{d}_{[\mathbf{m}]} = \mathbf{0} \tag{12}$$

where $\mathbf{k}_{\mathbf{e}[\mathbf{m}]}$ and $\mathbf{k}_{\mathbf{g}[\mathbf{m}]}$ are the elastic and geometric stiffness matrices for the segment, and $\mathbf{d}_{[\mathbf{m}]}$ is the displacement vector containing the displacement degrees of freedom for the given segment (which – at this point – are the Fourier coefficients). The $\mathbf{k}_{\mathbf{e}[\mathbf{m}]}$ matrix is derived from the internal potential (i.e., strain energy), while $\mathbf{k}_{\mathbf{g}[\mathbf{m}]}$ is derived from the external potential; hence, it is dependent on the involved stresses. Dependency of the geometric stiffness matrix on the stresses is linear, therefore it can be expressed as $\lambda \mathbf{k}_{\mathbf{g}[\mathbf{m}]}$ where λ is a load multiplier.

2.6 Stiffness matrices for the whole member

Unlike in a classic FEM, even one single segment in FTM might be enough to solve a tubular member, since applying longitudinal Fourier terms in large enough number can ensure a proper approximation of the displacement functions. However, since wind turbine towers are not uniform longitudinally, and/or they might be subjected to non-uniform loading, longitudinal discretization is considered here. The tubular member is assumed to be built up from uniform segments, and to each segment the above-described displacement approximation is applied. Within a segment, therefore, the procedure is exactly the one as described above.

Whenever there are multiple segments, it means two changes: (a) the size of the problem is increased, and (b) the segments must be joined. As far as (a) is concerned, if we have, e.g., g segments, then the displacement vector is composed of g partitions,

$$\mathbf{d}^{\mathbf{T}} = \begin{bmatrix} \mathbf{d}_{[\mathbf{1}]}{}^{\mathrm{T}} & \cdots & \mathbf{d}_{[\mathbf{m}]}{}^{\mathrm{T}} & \cdots & \mathbf{d}_{[\mathbf{g}]}{}^{\mathrm{T}} \end{bmatrix} \tag{13}$$

and the stiffness matrix is composed of $g \times g$ partitions:

$$\mathbf{K} = \begin{bmatrix} \mathbf{k}_{[\mathbf{1}]} & \cdots & \mathbf{0} & \cdots & \mathbf{0} \\ \vdots & \ddots & & & \vdots \\ \mathbf{0} & & \mathbf{k}_{[\mathbf{m}]} & & \mathbf{0} \\ \vdots & & & \ddots & \vdots \\ \mathbf{0} & \cdots & \mathbf{0} & \cdots & \mathbf{k}_{[\mathbf{g}]} \end{bmatrix} \tag{14}$$

Without considering the connections between the segments the off-diagonal terms are all zero. Further, the same scheme applies for both the elastic and the geometric stiffness matrices.

Regarding (b), the connection between the segments can be realized either by constraint equations or by springs (i.e., elastic links). Moreover, when the elastic stiffness matrix of the whole member is calculated, the effect of supports must also be considered. Two approaches are considered and implemented: by constraint equations and by discrete springs. All of these operations are briefly summarized as follows.

2.7 Joining segments by constraint equations

At locations where the two segments meet, the displacements (e.g., values of a translation function or any derivative of it) should be the same. For example, let us force identical u translation at a certain location at the common boundary of segment m and $m+1$, which location is identified by

the (common) x_{c1} position. This location has local longitudinal coordinates $y_{c1[m]} = L_{[m]}$ and $y_{c1[m+1]} = 0$, where $L_{[m]}$ is the length of the $[m]$-th segment. The constraint equation reads as:

$$\sum_{k=1}^{n} u_{k[m]} f_{k[m]}(x_{c1}, L_{[m]}) - \sum_{k=1}^{n} u_{k[m+1]} f_{k[m+1]}(x_{c1}, 0) = 0 \tag{15}$$

The above equation can be expressed in vector format, as follows:

$$[\ldots \quad f_{k[m]}(x_{c1}, L_{[m]}) \quad \ldots]\mathbf{d}_{[\mathbf{m}]} - [\ldots \quad f_{k[m+1]}(x_{c1}, 0) \quad \ldots]\mathbf{d}_{[\mathbf{m+1}]} = 0 \tag{16}$$

or, using the global displacement vector of the whole member (with multiple segments):

$$[\ldots \quad f_{k[m]}(x_{c1}, L_{[m]}) \quad \ldots \quad -f_{k[m+1]}(x_{c1}, 0) \quad \ldots]\mathbf{d} = 0 \tag{17}$$

Then further similar equations can be added to consider multiple locations between each of the adjoining segments, e.g.:

$$\begin{bmatrix} \ldots & f_{k[1]}(x_{c1}, L_{[m]}) & \ldots & -f_{k[2]}(x_{c1}, 0) & \ldots & & & & \\ \ldots & f_{k[1]}(x_{c2}, L_{[m]}) & \ldots & -f_{k[2]}(x_{c2}, 0) & \ldots & & & & \\ \ldots & f_{k[1]}(x_{c3}, L_{[m]}) & \ldots & -f_{k[2]}(x_{c3}, 0) & \ldots & & & & \\ & \vdots & & \vdots & & & & & \\ & & & & \ldots & f_{k[m]}(x_{c1}, L_{[m]}) & \ldots & -f_{k[m+1]}(x_{c1}, 0) & \ldots \\ & & & & \ldots & f_{k[m]}(x_{c2}, L_{[m]}) & \ldots & -f_{k[m+1]}(x_{c2}, 0) & \ldots \\ & & & & \ldots & f_{k[m]}(x_{c3}, L_{[m]}) & \ldots & -f_{k[m+1]}(x_{c3}, 0) & \ldots \\ & & & & & \vdots & & \vdots & \end{bmatrix} \mathbf{d} = \mathbf{0} \tag{18}$$

which can be written, in short, as:

$$\mathbf{Z_{join}}\mathbf{d} = \mathbf{0} \tag{19}$$

This means that the $\mathbf{d}$ displacement vector must lie in the null-space of $\mathbf{Z_{join}}$. The task is, therefore, to find a basis system for the null space. Note, the preceding procedure is general, i.e., the number of considered Fourier terms are not necessarily equal in the neighboring segments. Also, the same procedure could be followed for any point pairs, i.e., even if the point pairs are not located at the common location of two adjoining segments. Further, if the prescribed displacement is non-zero, the right side of Eq. (19) is a nonzero vector. In this case the equation system to be solved is a linear equation system, but it is indeterminate, and the solution is non-unique, and what we need to find is a basis system of all the possible solutions. Hence, mathematically, the task remains the same whether the prescribed displacement is zero or non-zero: determination of a basis system of a linear space.

2.8 Joining segments by elastic links

An alternative to constraint equations for connecting FTM segments is to use elastic links (i.e., linear springs) between the common boundary of two adjoining segments. If there is relative displacement between the two linked points a spring force is generated and when the spring is deformed, strain energy accumulates, that can then be considered in the potential functions. For now, consider the two points to be linked as located in two neighboring segments (elastic links can be added arbitrarily, even within segments, but our primary case here is segment to segment connection). For example, let us link the u translations at a certain location at the common boundary of segment m and $m+1$, which location is identified by the (common) x_{c1} position. This location has local longitudinal coordinates $y_{c1[m]} = L_{[m]}$ and $y_{c1[m+1]} = 0$, where $L_{[m]}$ is the length of the $[m]$-th segment. The relative displacement can be expressed as:

$$\Delta u_1 = \sum_{k=1}^{n} u_{k[m]} f_{k[m]}(x_{c1}, L_{[m]}) - \sum_{k=1}^{n} u_{k[m+1]} f_{k[m+1]}(x_{c1}, 0) \tag{20}$$

The above equation can be expressed in vector format, as follows:

$$\Delta u_1 = [\ldots \quad f_{k[m]}(x_{c1}, L_{[m]}) \quad \ldots]\mathbf{d}_{[\mathbf{m}]} - [\ldots \quad f_{k[m+1]}(x_{c1}, 0) \quad \ldots]\mathbf{d}_{[\mathbf{m+1}]} \tag{21}$$

or, using the global displacement vector of the whole member (with multiple segments):

$$\Delta u_1 = [\ldots \quad f_{k[m]}(x_{c1}, L_{[m]}) \quad \ldots \quad -f_{k[m+1]}(x_{c1}, 0) \quad \ldots]\mathbf{d} \tag{22}$$

If the stiffness of the spring stiffness is k_1, the associated energy is:

$$\Pi_{link,1} = \frac{1}{2} k_1 \, [\Delta u_1]^2 \tag{23}$$

If there are multiple links between the two segments, e.g., *nc* in total, the above energy terms must be summarized.

$$\Pi_{link} = \sum_{ic=1}^{nc} \frac{1}{2} k_{ic} \left[\sum_{k=1}^{n} u_{k[m]} f_{k[m]}(x_{ic}, L_{[m]}) - \sum_{k=1}^{n} u_{k[m+1]} f_{k[m+1]}(x_{ic}, 0)\right]^2 \tag{24}$$

The spring energy is added to the internal potential, and – after taking the derivatives – it leads to a supplement to the partition of the global stiffness matrix which is associated with the degrees of freedom of the [*m*] and [*m*+1] segments. Hence, if we look at this partition, it is modified as follows:

$$\begin{bmatrix} \mathbf{k_{e[m]}} & \mathbf{0} \\ \mathbf{0} & \mathbf{k_{e[m+1]}} \end{bmatrix} \rightarrow \begin{bmatrix} \mathbf{k_{e[m]}} & \mathbf{0} \\ \mathbf{0} & \mathbf{k_{e[m+1]}} \end{bmatrix} + \begin{bmatrix} \mathbf{k_{link[m]}} & \mathbf{k_{link[m,m+1]}} \\ \mathbf{k_{link[m+1,m]}} & \mathbf{k_{link[m+1]}} \end{bmatrix} \tag{25}$$

Note, the $\mathbf{k_{link}}$ matrices are full matrices. Further, if the spring rigidity is large enough, the elastic link can create a practically rigid link.

2.9 Rigid supports by constraint equations

Constraint equations can be applied to ensure zero (or: arbitrary non-zero but prescribed) displacement or a displacement derivative at a given, arbitrary locations. Let us assume that a certain *d* displacement component is zero at a specific location (x_{s1}, y_{s1}) in the *m*-th segment. Since the displacement is expressed by linear combination,

$$d(x_{s1}, y_{s1}) = \sum_{k=1}^{n} d_k f_{k[m]}(x_{s1}, y_{s1}) = 0 \tag{26}$$

This equation – typically – does not make any d_k coefficient equal to zero, but it does mean that the d_k coefficients are not independent of each other. The equation can be written in vector form:

$$[\ldots \quad f_{k[m]}(x_{s1}, y_{s1}) \quad \ldots]\mathbf{d} = 0 \tag{27}$$

where $\mathbf{d}$ is the vector of Fourier coefficients, and the first row vector contains the function terms considered in the displacement approximation with their substitution values at (x_{s1}, y_{s1}). If zero displacement is prescribed in multiple locations, there are multiple equations, which can be summarized as:

$$\begin{bmatrix} \cdots & f_{k[1]}(x_{s1},y_{s1}) & \cdots & & & & \\ \cdots & f_{k[1]}(x_{s2},y_{s2}) & \cdots & & & & \\ \cdots & f_{k[1]}(x_{s3},y_{s3}) & \cdots & & & & \\ & \vdots & & & & & \\ & & & \cdots & f_{k[m]}(x_{s1},y_{s1}) & \cdots & \\ & & & \cdots & f_{k[m]}(x_{s2},y_{s2}) & \cdots & \\ & & & \cdots & f_{k[m]}(x_{s3},y_{s3}) & \cdots & \\ & & & & \vdots & & \\ & & & & & etc. & \end{bmatrix} \mathbf{d} = \mathbf{0} \tag{28}$$

which can be written, in short, as:

$$\mathbf{Z_{sup}d} = \mathbf{0} \tag{29}$$

This means that the $\boldsymbol{d}$ displacement vector must lie in the null-space of $\boldsymbol{Z_{sup}}$. The task is, therefore, to find a basis system for the null space.

2.10 Supports by elastic links

Linear elastic springs can be defined at arbitrary positions over the cylindrical surface. If they are present, additional stiffness terms are to be added to the elastic stiffness matrix. The displacement at a support location generates a reaction force. When the spring is deformed, strain energy accumulates, which is to be considered in the potential function. If a spring (#1) is located in the m-th segment at (x_{s1}, y_{s1}), and its stiffness is k_1, the associated energy is:

$$\Pi_{sup,1} = \frac{1}{2} k_1 \left[d\left(x_{s,1}, y_{s,1}\right) \right]^2 = \frac{1}{2} k_1 \left[\sum_{k=1}^{n} d_k f_{k[m]}(x_{s,1}, y_{s,1}) \right]^2 \tag{30}$$

If there are multiple spring supports in the m-th segment, e.g., ns in total, the above energy terms must be summed.

$$\Pi_{sup} = \sum_{is=1}^{ns} \Pi_{sup,is} = \sum_{is=1}^{ns} \frac{1}{2} k_{is} \left[\sum_{k=1}^{n} d_k f_{k[m]}(x_{s,is}, y_{s,is}) \right]^2 \tag{31}$$

The spring energy is added to the internal potential, and – after taking the derivatives – it leads to a supplement to the elastic stiffness matrix of the given segment: $\mathbf{k_{sup[m]}}$.

$$\mathbf{k_{e[m]}} \rightarrow \mathbf{k_{e[m]}} + \mathbf{k_{sup[m]}} \tag{32}$$

Note, $\mathbf{k_{sup[m]}}$ is a full matrix if $(x_{s,is}, y_{s,is})$ position is arbitrary, even if one single spring support is defined (though certain elements or partitions of $\mathbf{k_{sup[m]}}$ can be zero if the support is located at the zero point of some f_k basis functions). Thus adding even a single spring support transforms the elastic stiffness matrix of the segment into a (nearly) fully populated matrix (which is rather different from the situation in a typical finite element implementation, but follows from the nature of the Fourier-series approximations in FTM as opposed to spline-like approximations used in FEM).

2.11 DOF transformation due to constraint equations

If rigid connections are to be modelled, there is little difference between the practical applicability of constraint equations and elastic links. A potential benefit of using elastic links is that elastic (i.e., not fully rigid) connection can readily be defined. A potential benefit of the constraint

equation approach is that the problem size is slightly reduced, which however, is associated with DOF transformation.

When constraint equations are applied, either to join the segments or to consider supports, the problem, mathematically, is the same: we need to find a basis system for a linear space. Joining the segments and considering the supports, therefore, can be completed in one step, as follows. For the sake of simplicity let us assume that zero displacements are prescribed at the support locations. Eqs. (19) and (29) can be expressed by a single matrix equation as follows:

$$\begin{bmatrix}\mathbf{Z_{join}}\\ \mathbf{Z_{sup}}\end{bmatrix}\mathbf{d} = \mathbf{Z}\mathbf{d} = \mathbf{0} \tag{33}$$

Solving the $\mathbf{Zd} = \mathbf{0}$ equation leads to a basis system of the null-space:

$$\mathbf{Q} = null(\mathbf{Zd}) \tag{34}$$

where the column vectors of the $\mathbf{Q}$ matrix are the basis vectors of the null space. The number of column vectors – in any reasonable case – is less than the number of original Fourier coefficients, thus, considering the supports and joining the segments result in a reduction of the degrees of freedom of the problem. The new degrees of freedom are not Fourier coefficients any more, but still can be summarized in a displacement vector $\mathbf{d_{red}}$. The relationship between the Fourier coefficients and the new displacement vectors is:

$$\mathbf{d} = \mathbf{Q}\mathbf{d_{red}} \tag{35}$$

2.12 Buckling analysis

To solve the FTM buckling problem the practical steps are as follows. First, we need to calculate the stiffness matrices according to Section 2.4. If there are multiple segments, we need $\mathbf{k_{e[m]}}$ and $\mathbf{k_{g[m]}}$ for each segment. Then, if spring supports are considered, we need to add $\mathbf{k_{sup[m]}}$ to $\mathbf{k_{e[m]}}$, as in Eq. (32). Next, we need to create the stiffness matrix for the whole member, as expressed by Eq. (14). If elastic links are present, we need to add the $\mathbf{k_{link}}$ matrices to the global stiffness matrix, according to the scheme shown by Eq. (25). Finally, the buckling problem can be expressed similarly to Eq. (12), but now for the whole member:

$$\left(\mathbf{K_e} - \lambda\mathbf{K_g}\right)\mathbf{d} = \mathbf{0} \tag{36}$$

where $\mathbf{K_e}$ and $\mathbf{K_g}$ is the stiffness matrices for the whole member, and $\mathbf{d}$ is the displacement vector for the whole member, containing the displacement degrees of freedom for the whole member (which are the Fourier coefficients, unless constraint equations are involved).

If we have constraint equations, we need to find the $\mathbf{Q}$ transformation matrix per Eq. (34) and the $\mathbf{d}$ vector must be transformed. In this case substituting Eq. (35) into Eq. (36):

$$\left(\mathbf{K_e} - \lambda\mathbf{K_g}\right)\mathbf{Q}\mathbf{d_{red}} = \mathbf{0} \tag{37}$$

Then, pre-multiplying by $\mathbf{Q}^{\mathrm{T}}$ and rearranging, we have:

$$\mathbf{Q}^{\mathrm{T}}\mathbf{K_e}\mathbf{Q}\mathbf{d_{red}} - \mathbf{Q}^{\mathrm{T}}\mathbf{K_g}\mathbf{Q}\mathbf{d_{red}}\lambda = \mathbf{0} \tag{38}$$

which can be recognized as a generalized eigen-value problem, expressed in the transformed space.

$$\mathbf{K_{e,red}}\mathbf{d_{red}} - \mathbf{K_{g,red}}\mathbf{d_{red}}\lambda = \mathbf{0} \tag{39}$$

where $\mathbf{d_{red}}$ is the final, reduced displacement vector, and $\mathbf{K_{e,red}}$ and $\mathbf{K_{g,red}}$ are final, reduced stiffness matrices for the member with multiple segments and considering elastic supports and/or links as well as constraint equations.

When the eigenvalue problem is solved, it leads to the eigenvalues and eigenvectors, i.e., specific pairs of λ and $\mathbf{d_{red}}$. Since $\mathbf{d_{red}}$ is a displacement vector, it defines the shape of the member, i.e. the buckling (or mode) shape. λ is a load multiplier, usually termed as the critical load (or critical load factor/multiplier). The eigenvalue problem has as many possible solutions as degrees of freedom (though not all solutions are positive or real). Accordingly, it is common to express the family of all eigen-buckling solutions as:

$$\mathbf{K_{e,red}\Phi - K_{g,red}\Phi\Lambda = 0} \tag{40}$$

where $\mathbf{\Phi}$ is a matrix with all the eigen-vectors (i.e., displacement vectors) in its columns, and $\mathbf{\Lambda}$ is a diagonal matrix which contains all the corresponding λ critical load multipliers.

3. Validation and illustration through examples

The developed method is able to perform linear buckling analysis for a wide range of problems, for pure or combined loading, with virtually arbitrary supports, and for a wide range of tube geometries. The numerical experience is that the necessary number of Fourier terms is small, i.e., the resulting number of displacement degrees of freedom (DOFs) is much smaller compared to that required in a shell FEM analysis. However, what Fourier terms are "necessary" is strongly dependent on the problem; namely, it is dependent on the load type, on the member length, on the support conditions, and on whether we want to focus on the first buckling mode only or want to have higher modes too. In the following subsections sample results are shown. In all the examples standard isotropic steel properties are used: E = 210 GPa, ν = 0.3. Moreover, in most examples 1 mm wall thickness is used; hence, if not stated otherwise, t=1 mm. Most examples were calculated by both FTM versions (i.e., sin-cos and sin-only), and it was concluded that the differences between the results from the two versions are negligible. The actual numerical values presented are taken from the sin-only version.

3.1 Pure load cases, first buckling mode, single segment

To study the first buckling modes, we have considered tubes with globally and locally pinned end supports, with a wide range of R/t ratios between 10 and 500, as well as with an extremely wide length range. (Note, according to [19] practical wind turbine tower segments are characterized by R/t between 30 and 150; typical L/R ratio for a tower segment is between 5 and 20, while it is between 40 and 70 for a whole tower.) In Fig. 2 the first-mode critical loads for pure N load are plotted with respect to member length. Sample buckling shapes are presented for the case of R=50 mm, and L=10, 50, 200, 1000, and 2000 mm. (The coloring is based on the w radial displacement.) In Fig. 3 the first-mode critical loads for pure M moment are plotted with respect to member length. Sample buckling shapes are presented for the case of R=50 mm, and L=10, 50, 200, and 10000 mm. In Fig. 4 the first-mode results are presented, for pure T. The buckled shapes are for R=10 mm, and L=2, 5, 10, 50, 1000, and 5000 mm.

Finally, pure V is shown in Fig. 5. The buckled shapes are for R=50 mm, and L=10, 50, 500, 2500, and 25000 mm.

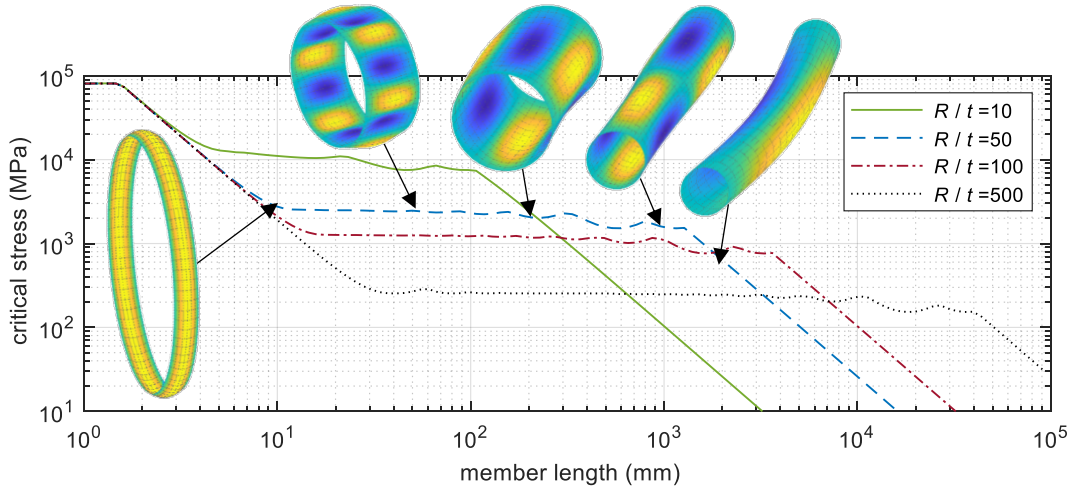

Figure 2: Pure N

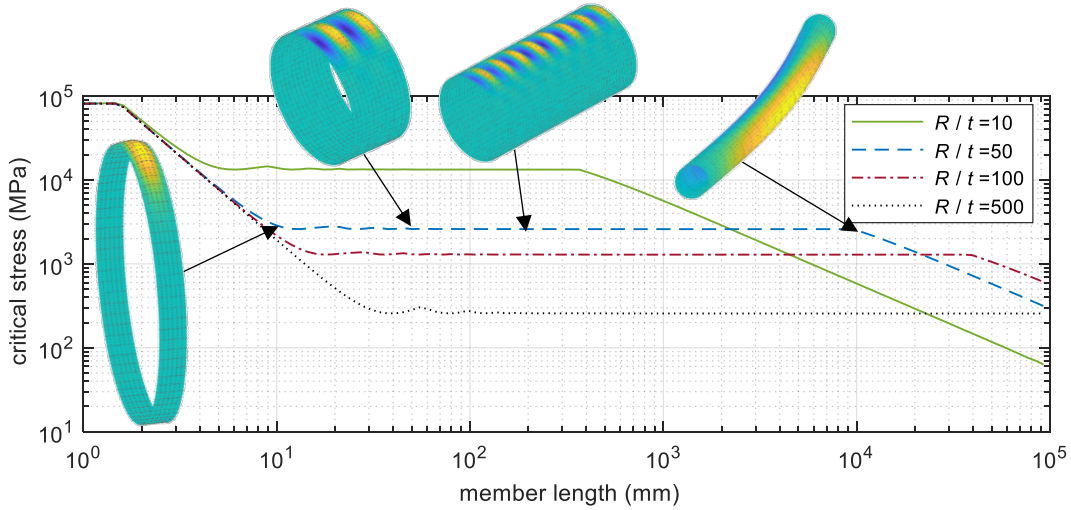

Figure 3: Pure M

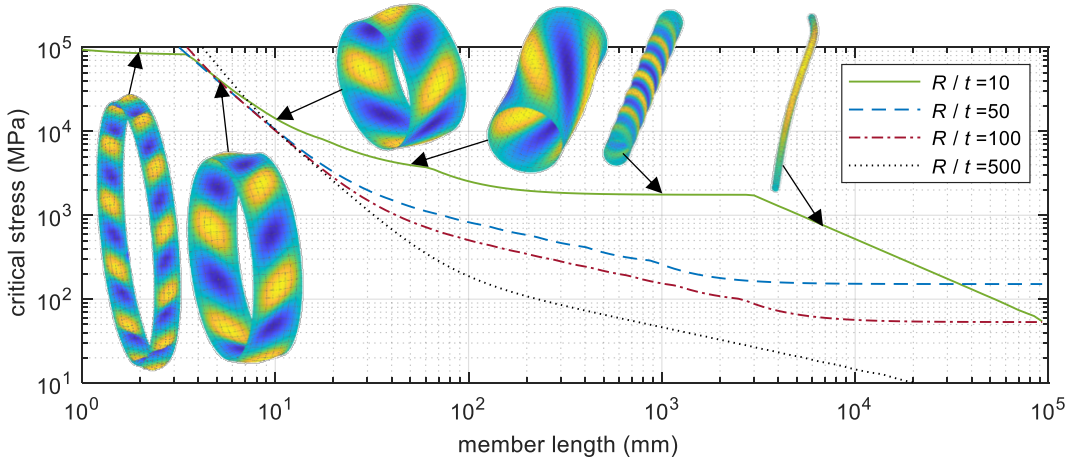

Figure 4: Pure T

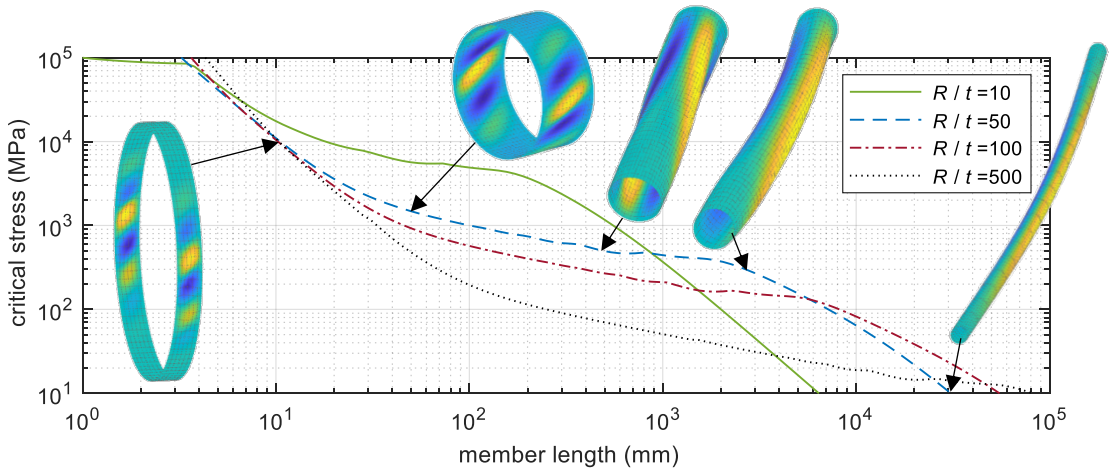

Figure 5: Pure V

As shown in the figures, FTM is capable of predicting the full range of buckling behavior for primary loading actions. In the case of 'pure N' (axial), the well-known buckling results are reproduced: if the member is very short, the barrel-type (axisymmetric) mode controls (L mode), for large lengths the member buckles in a global flexural mode (F mode), while for a wide range of intermediate lengths we observe the shell-shaped (S mode) buckling lobes, with a varying number of circumferential and meridian lobes.

In the case of 'pure M', unless the member is extremely long, the first buckling mode is characterized by one single circumferential lobe at the compressed part of the tube (L mode): if the member is very short, there is one single meridian lobe, otherwise the number of meridian lobes is proportional to the member length (while the half-wavelength and critical load being nearly constant). Though it is rarely reported in the literature, a global mode does exist, which is a lateral-torsional (LT) buckling mode, but with very small twist. However, this global mode is first only if the member is extremely long (e.g., if R=100 mm and t=1 mm, the member length should be more than 100 m!); so the mode has little practical relevance.

In the case of 'pure T', at very large lengths the buckling is global, i.e., without cross-section distortion; and the shape of the longitudinal system line is helical (H mode). For lengths smaller than required to have helical buckling, usually there is a plateau in the curve: in this length range the inclination of the buckling lobe is constant, and two lobes are spiraling longitudinally (S2 mode). If the member length is smaller, the lowest buckling mode is characterized by one lobe in the longitudinal direction, while the number of circumferential lobes is inversely proportional to the member length (S1 mode). In the case of short members, the inclination of the buckling lobes is approx. 45 degrees, and as the member length increases, the lobes are less and less inclined (w.r.t. the longitudinal axis).

In the case of 'pure V' the behavior is essentially similar to that for 'pure T'. Unless the member length is very large, there are multiple circumferential lobes; however, they are not uniform along the circumference (S mode) but located where the maximum shear stresses occur. It is little known (if reported at all) that global buckling mode exists if the member is sufficiently long. This global mode is visually similar to a flexural buckling mode in the lateral direction (i.e., with translations perpendicularly to the shear force).

3.2 Pure load cases, comparison to analytical and FEM solutions

For validation, the FTM results are compared to analytical and shell FEM resultsfor the cases of pure N, pure M, and pure T. Across these caes ranges of R and L values are considered (while keeping the thickness 1 mm) in order to generate all the characteristic buckling types. In all the calculations the ends are simply supported.

Analytical solutions exist for the various typical buckling modes for all N, M and T, though some of the analytical solutions are decidedly approximate. The analytical formulae used for the validation are summarized in Appendix C. (Note, we do not know of any analytical solution for pure V, although the effect of shear was investigated by a number of researchers.)

For shell FEM the Abaqus [23] software package is employed. S4R linear shell elements are used. The discretization strongly varies, in order to achieve reasonably accurate results and within a reasonable calculation time. (Note that the resulting total number of DOF varies from ~10 thousand to ~1 million.) Loads are applied as shell edge loads to minimize local effects.

Comparison of FTM to analytical and FEM results are summarized in Tables 1 to 3.

Regarding FTM vs. shell FEM, the agreement is mostly excellent There are slightly larger differences if the member is very short and the R/t is small, which can be attributed to the effect of supports and the effect of differences in the underlying mechanics (most importantly: FTM does not consider through-thickness shear deformations, while the employed shell FEM does). Moreover, some differences are experienced in the case of helical buckling if the radius is large, in these cases the member lengths are extreme, and both FTM and FEM calculations can be supposed to be subjected to numerical inaccuracies.

If the load is pure N, the agreement between the FTM and analytical/FEM results is excellent, for all the mode types. In the case of local buckling of pure M, the typical analytical solution is an upper bound approximation (as the numerical results in Table 2 show). It is also observable, that: the thinner the shell is, the better the analytical approximation is. In the case of LT buckling the agreement is very good. In the case of local buckling under pure T, Donnell's solution is employed for the S1 mode, while Flügge's solution is employed for the S2 mode. According to Table 3, both Donnell's and Flügge's solutions are slightly approximate. In the case of global buckling the FTM and FEM solutions are systematically smaller compared to the analytical solution from Greenhill, the latter one leading to approx. 20% larger critical loads. This difference can be explained, but it is beyond the limits of the actual paper.

Table 1: Critical stresses for pure N

R mm	L mm	FTM N/mm^2	ana./ FTM	FEM/ FTM	buckl type
10	10.93	10882	0.98	1.00	S
10	15	10449	1.00	1.02	S
10	50	7550	1.02	1.03	S
10	200	2427	1.01	1.01	F
10	1000	103.5	1.00	0.98	F
50	36.66	2488	0.99	0.99	S
50	100	2298	1.01	1.02	S
50	500	1566	1.01	1.01	S
50	2000	636.7	1.00	1.00	F
50	5000	103.5	1.00	1.00	F

100	51.85	1252	1.00	1.00	S
100	500	1145	1.00	1.01	S
100	1500	770.7	1.00	1.00	S
100	5000	410.0	1.00	1.00	F
100	10000	103.5	1.00	1.00	F
500	115.9	253.6	1.00	1.00	S
500	1000	246.7	1.00	1.00	S
500	20000	154.6	1.00	1.00	S
500	50000	103.3	1.00	1.00	F
500	100000	25.89	1.00	1.00	F

Table 2: Critical stresses for pure M

R mm	*L* mm	FTM N/mm^2	ana./ FTM	FEM/ FTM	buckl type
10	27.33	13456	0.94	0.95	L
10	1000	5646	1.02	1.00	LT
10	5000	1159	1.00	0.99	LT
50	61.10	2604	0.98	0.99	L
50	10000	2514	1.01	1.00	LT
50	50000	575.0	1.01	0.99	LT
100	86.41	1291	0.98	1.00	L
100	100000	564.2	1.03	1.00	LT
500	193.2	256.2	0.99	1.00	L

Table 3: Critical stresses for pure T

R mm	*L* mm	FTM N/mm^2	ana./ FTM	FEM/ FTM	buckl type
10	10	14610	1.10	1.08	S1
10	50	4105	1.02	1.00	S1
10	400	1816	0.93	1.00	S2
10	2000	1756	0.96	1.00	S2
10	6000	865.9	1.27	0.99	H
10	10000	521.0	1.27	0.99	H
50	50	1350	1.07	1.08	S1
50	250	559.9	0.96	1.01	S1
50	1000	287.6	0.92	1.00	S1
50	5000	156.7	0.96	1.01	S2
50	10000	152.7	0.98	1.01	S2
50	300000	87.44	1.26	0.97	H
100	100	535.7	1.05	1.04	S1
100	500	235.9	0.95	1.00	S1
100	2000	116.8	0.95	1.00	S1
100	20000	54.27	0.98	1.00	S2
100	50000	53.46	0.99	1.00	S2

100	1500000	37.44	1.17	0.95	H
500	500	69.60	0.99	1.03	S1
500	1000	49.70	0.96	1.01	S1
500	10000	16.21	0.91	1.00	S1

3.3 Pure load cases, higher buckling modes

Calculation of higher buckling modes is obviously possible by FTM. The only practical issue is that higher modes typically require more longitudinal terms to provide sufficient precision. The number of necessary Fourier terms is also dependent on how many modes are intended to be calculated. As an example, Fig. 6 shows how the critical loads increase with mode number, in the case of various pure loads. The plots show the first 500 modes for a tubular member with R = 10, 50, 100, and 500 mm, t = 1 mm. The length is 8×R. The ends are simply supported.

Cylindrical shells are infamous for having large number of buckling modes with nearly identical critical loads. This is true for pure N and pure M if the shell is thin. In other situations, the critical load values increase much more rapidly as higher modes are considered. Two other small observations from the figure: (i) critical normal stress to M is always larger than that to pure N, and (ii) critical shear stress to V is always larger than that to pure T.

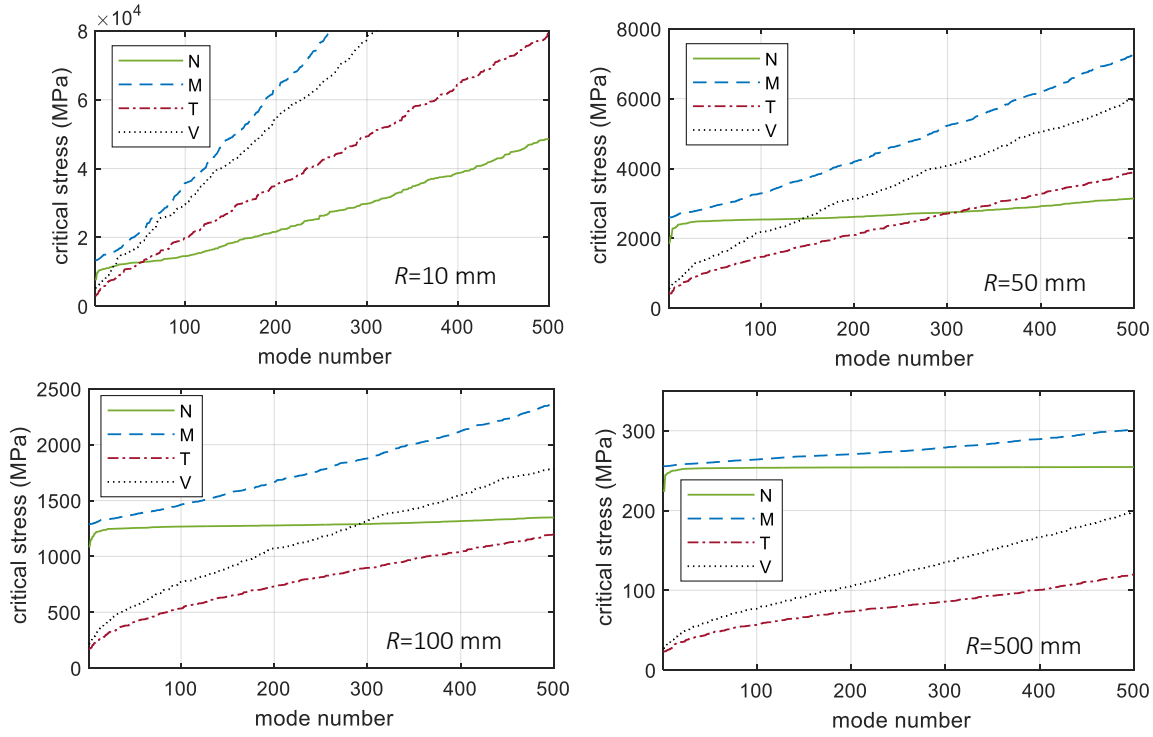

Figure 6: Critical stresses for higher buckling modes

3.4 Combined load cases, first buckling mode

As highlighted in the Introduction, the presented research was motivated by wind turbine towers, which are subjected to a combination of various internal actions, see e.g. [19,24], therefore, it is of

high importance to be able to handle combined loading. Moreover, the combination of actions strongly varies along the length of the tower.

The change of the buckling shape under combined actions is illustrated in Fig. 7, where the M+T interaction is presented for a tube with $R = 100$ mm, $t = 1$ mm, $L = 600$ mm. In the figure, e.g., $0.2M_{cr}+0.8T_{cr}$ should be interpreted as the stress in the member is combined from 0.2 times the critical stress to pure M and 0.8 times the critical stress to pure T. The leftmost figure shows the pure torsion case, the rightmost figure belongs to pure M. The pure T shape is point-symmetric, but even a small M destroys the point-symmetry, and the buckling waves more and more move toward the compressed part of the member as M increases (from left to right). At around $0.2M_{cr}$ the tensioned part becomes practically free of buckling lobes; and this shape remains hardly changed till approx. $0.7M_{cr}$. Then, the inclination of the lobes starts to increase, till $0.78M_{cr}$. Between $0.780M_{cr}$ and $0.781M_{cr}$ there is a sudden change of the shape. At $0.781M_{cr}$ the shape is already similar to the pure M shape, though the lobes are slightly inclined, which inclination decreases to zero as the torsion component decreases to zero.

In Fig. 7 the critical load factors (denoted as 'lf') are also given. In Fig. 8 these critical load factors are plotted in a classic interaction diagram. The M/M_{cr} (or: T/T_{cr}) ratio where the sudden shape change occurs coincides the break point in the interaction curve. This, also, indicates that there is a switch in the mechanics of the first buckling mode.

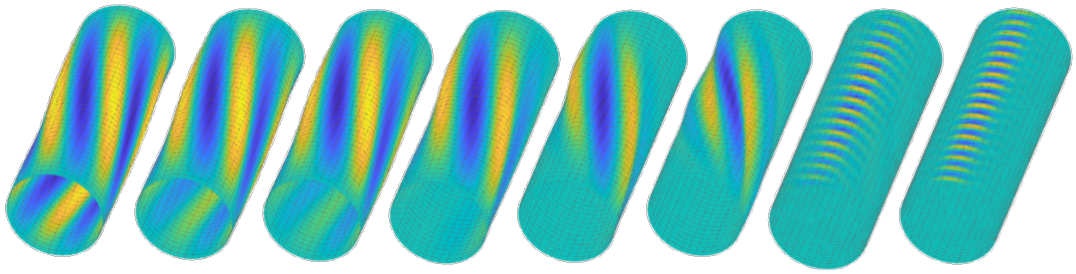

$0.0M_{cr}$	$0.03M_{cr}$	$0.05M_{cr}$	$0.2M_{cr}$	$0.7M_{cr}$	$0.780M_{cr}$	$0.781M_{cr}$	$1.0M_{cr}$
$1.0T_{cr}$	$0.97T_{cr}$	$0.95T_{cr}$	$0.8T_{cr}$	$0.3T_{cr}$	$0.220T_{cr}$	$0.219T_{cr}$	$0.0T_{cr}$
lf=1	lf=1.026	lf=1.041	lf=1.116	lf=1.266	lf=1.268	lf=1.267	lf=1

Figure 7: Combined loading, R=100, t=1, L=600 (pinned)

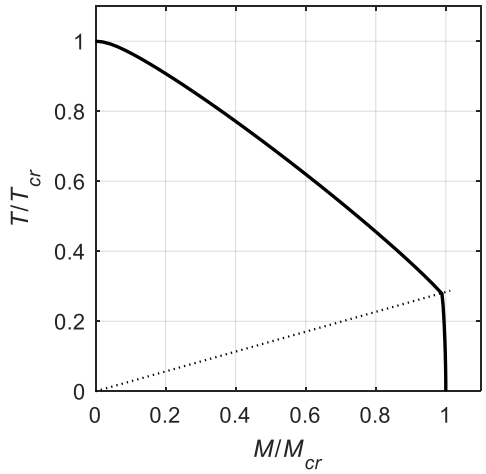

Figure 8: Combined loading, R=100, t=1, L=600 (pinned), M+T interaction curve (dotted line: 0.781M+0.219T)

In Fig. 9 three-dimensional buckling load interaction surfaces for combined loads are presented for two tubular members: (i) for $R = 50$ mm, $t = 1$ mm, $L = 300$ mm, and (ii) for $R = 100$ mm, $t = 1$ mm, $L = 600$ mm under N, M, V, and T actions. The surfaces represent the critical load factors, calculated by systematically varying the ratio of 3 selected loads (while keeping the fourth one equal to zero). The surface is generated by using normalized stress magnitudes as loading, so that the buckling load factor for the pure cases are equal to one. The coloring of the surface is based on the distance of the surface point from the plane of linear interaction (determined by the pure load points at the coordinate axes).

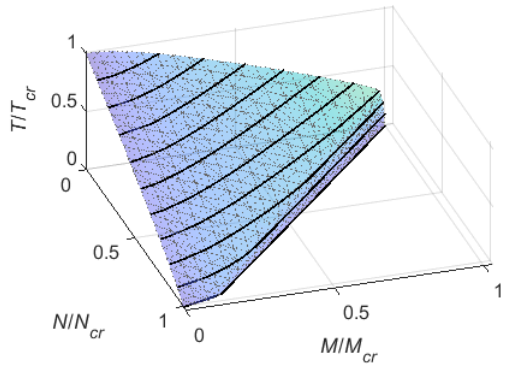

50-1-300-NMT

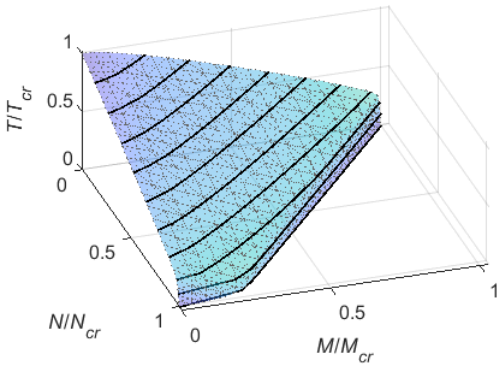

100-1-600-NMT

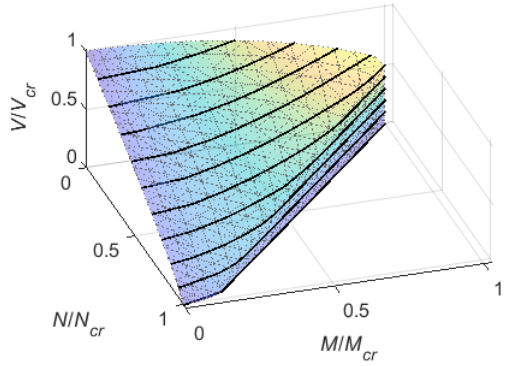

50-1-300-NMV

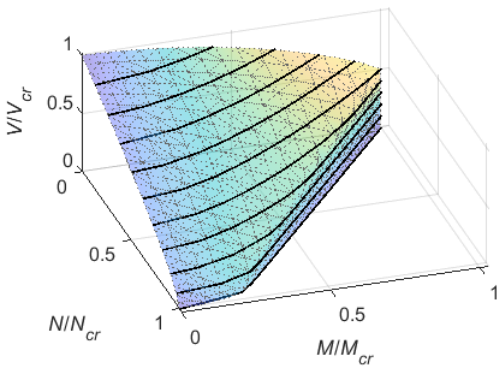

100-1-600-NMV

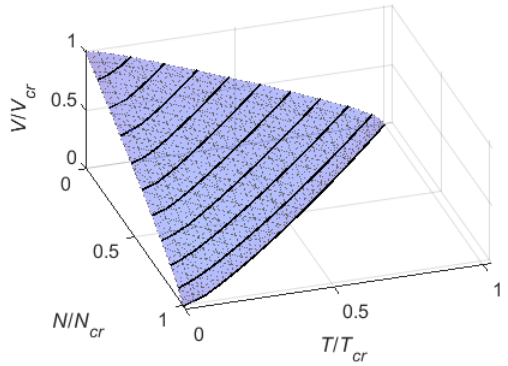

50-1-300-NTV

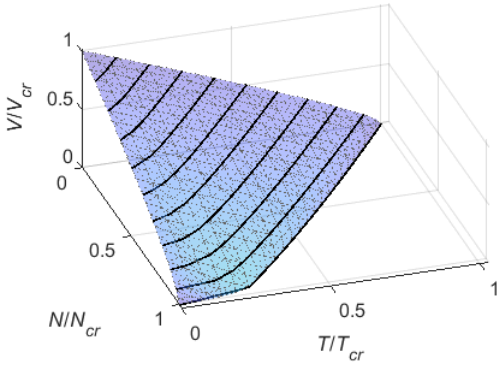

100-1-600-NTV

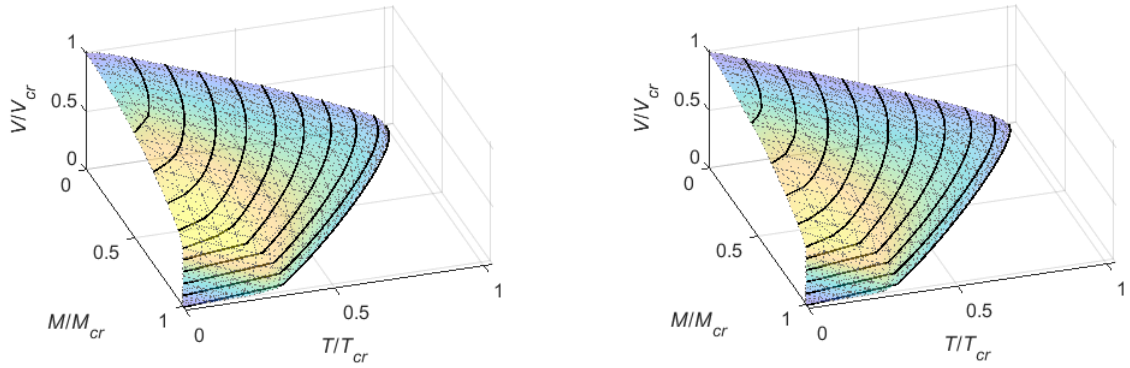

Figure 9: Interaction diagrams for various load combinations

From the numerical studies it is observed that the handling of combined loading does not provide any particular difficulty. The interaction surface is nonlinear, thus the stability of a tube under combined loading is best considered under the actual loading state, as opposed to simple superposition of the pure load cases (as is common in design). The interaction between the load cases varies: and it primarily depends on the loads, but influenced by the tube geometry, too.

3.5 Uniform geometry, nonuniform loading

Two cantilevered tubes of uniform geometry are considered here: (#1) under self-weight loading, and (#2) under end-loaded N, V, and T. In the case of Cantilever #1, the tube has R = 100 mm, t = 1 mm, and L = 200, 800, or 1200 mm are considered. The tube is assumed to be a horizontal cantilever, subjected to its own self-weight as loading as depicted in Fig. 10. Assuming a steel tube with a mass density of 7850 kg/m^3, and g of 9.81 m/s^2, the resulting vertical body load is 77.0 kN/m^3, equivalent to a 0.0484 kN/m uniformly distributed line load. The material is elastic and isotropic, with E=210000 MPa and Poisson's ratio of 0.3.

The linear buckling problem is solved by FTM and by shell FEM in Abaqus. In the case of the shell FEM, S4R linear shell elements are used with aspect ratio maintained near one. In the circumferential direction 314 elements are applied, hence the element size is 2×2 mm. This is a dense enough discretization per [6] since elements are equal to $0.2\sqrt{Rt}$. Loads are applied as shell surface loads (i.e., the self-weight is converted into tangential surface load, in order to avoid localized bending and/or minimize the hoop stresses).

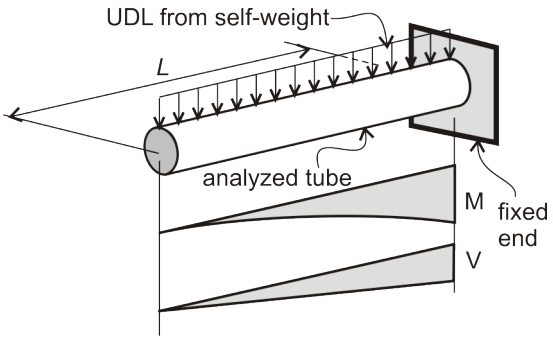

Figure 10: Arrangement for Cantilever #1

The critical load factors and the buckling mode shapes are shown in Fig. 11. (To better visualize the buckling shape, the cantilever is reversed so that the compressed part is on the top.) When the cantilever is short, the behavior is dominated by shear: and the buckled shape is similar to pure shear buckling. When the cantilever is long (e.g., 1200 mm in this example), the bucking shape is similar to pure M buckling: the buckling lobes are concentrated at the fixed end at the most compressed part of the cross-section. For intermediate lengths a gradual change from quasi-pure-V to quasi-pure-M can be observed, illustrated by the 800-mm-long member: the buckling lobes are concentrated around the most compressed part of the member, but they cover a larger area (compared to pure M), and inclined lobes are clearly visible (characteristic of V loading). As can be observed, the agreement between the FTM and shell FEM is excellent, the differences are practically negligible. In the case of FTM no longitudinal (segment-to-segment) discretization is necessary to solve this problem, and in fact, has not been applied. Nevertheless, a relatively large number of longitudinal Fourier-terms is required (i.e., large value for q, see Appendix A), since the characteristic length of the buckling lobes is short; however, the FTM DOF is still much smaller compared to shell FEM. (It is to note that though in these examples the DOF number ratio between FEM and FTM is approximately 100 to 1, the actual ratio is dependent on the analyzed problem. Still, it is safe to assume that FTM operates with significantly fewer degrees of freedom compared to shell FEM.)

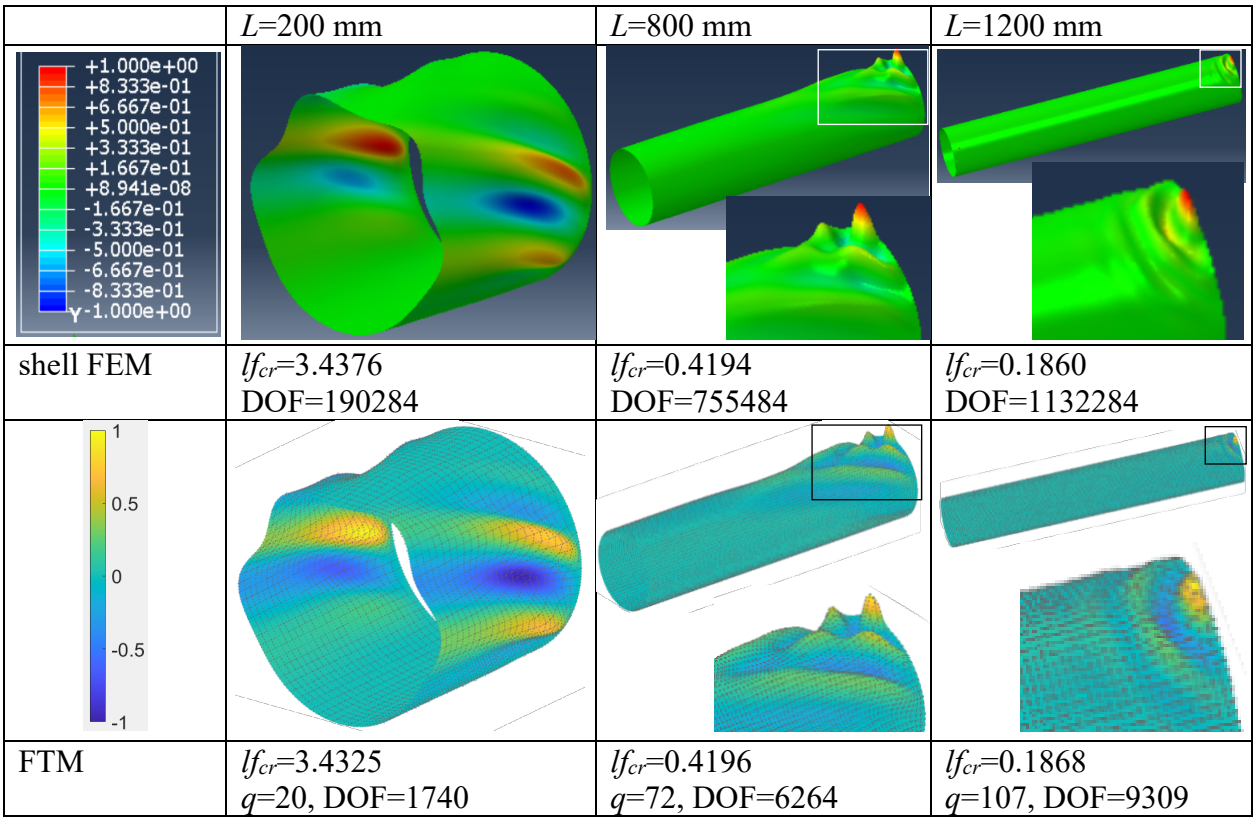

Figure 11: Cantilever #1, buckled shapes, critical load factors

Cantilever #2 also has uniform geometry, but with non-uniform loading created by end-loading as depicted in Fig. 12. The arrangement is essentially identical to one of the cases recently

experimentally tested [24]. The F force has a horizontal eccentricity (e), from which the member is subjected to a constant torque, so that the T/M ratio at the fixed end of the cantilever is equal to 1/3. The analyzed steel tube has an R=125 mm, t=0.79 mm, a length L=750 mm. The vertical force in the test program was applied through a rigid extension attached to the end of the tube, so that the lever arm to calculate the maximal M bending moment is $L_{tot}=L+L_{ext}$ =750+150=900 mm. An axial compressive force, N=F, is also considered here, but was not applied in the experimental program. The arrangement is shown in Fig. 13.

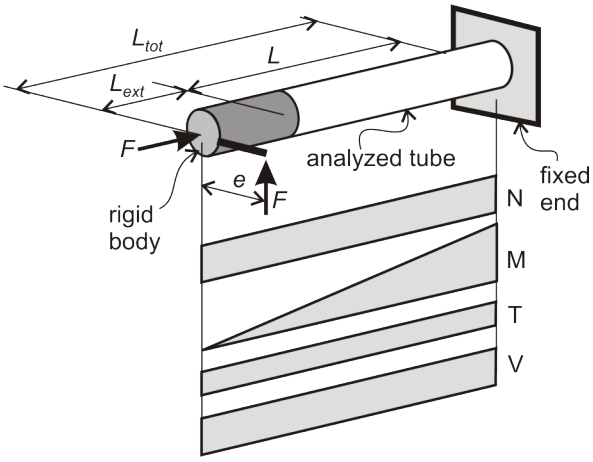

Figure 12: Arrangement for Cantilever #2

Cantilever #2 is analyzed by FTM, and the buckling analysis performed for various combinations of the stresses, starting from the basic isolated cases and then leading to the fully combined N, M, T, and V, with the main results summarized in Fig. 13. Note, in the experimental program a stiff end-plate was attached to the tube at both ends. At the fixed support the end-plate was bolted to a rigid testing frame, while at the free end load was applied. In the FTM the end-plates are not directly modelled; instead, at the fixed end the tube cross-section is rigidly supported, and at the free end a quasi-rigid tube segment was attached to approximate the loading apparatus. Note, in the response plots in Fig. 13 the quasi-rigid end is not shown.

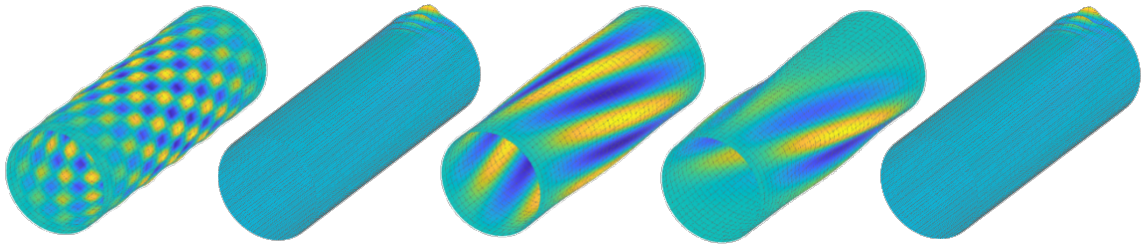

N	M	T	V	M+N
F_{cr} = 491.7 kN	F_{cr} = 31.63 kN	F_{cr} = 27.02 kN	F_{cr} = 47.08 kN	F_{cr} = 29.78 kN

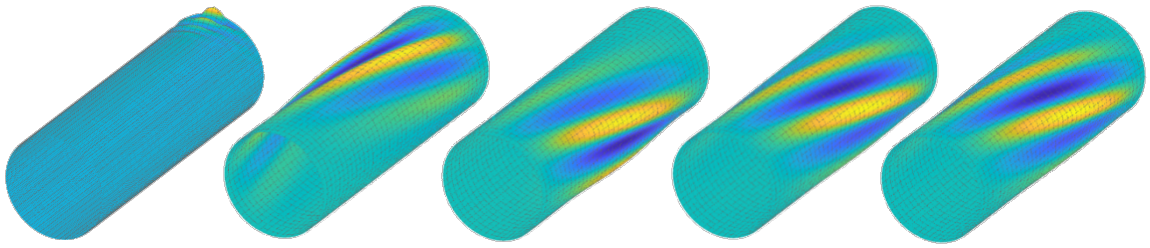

M+V	M+T	T+V	M+T+V	M+T+V+N
F_{cr} = 31.51 kN	F_{cr} = 20.20 kN	F_{cr} = 17.99 kN	F_{cr} = 17.00 kN	F_{cr} = 16.54 kN

Figure 13: Cantilever, R=125, t=0.79, L=750, T/M=1/3

Fig. 13 provides a wealth of information about the response of this cantilevered tube to an end-load, and examining the value of the end-loaded F_{cr} and the buckling shape under different isolated and combined cases provides a means to understand how the buckling load and shape are influenced by the various combinations. Importantly, in the studied example, in considering the combined M+T+V+N case (i) buckling (load factor and shape) is primarily determined by the shear stresses from T and V, (ii) T and V have roughly equal importance, (iii) the value of the critical force is slightly reduced by the presence of normal stresses from M and N, (iv) the shape of the buckling lobes is determined primarily by T and V, that is why the buckling lobes are inclined, and (v) the location of the buckling lobes coincide with the location of the largest principal compressive stresses.

In the design of steel structural members the effect of shear force (V) is frequently neglected, which practice seems to be approximately confirmed here by looking at the M+V case. However, if V and T (i.e., the two load cases from which shear stress is derived) are combined, the important effect of V can be observed both from the buckled shape and the associated critical force. Though it is unusual to define 'pure V' as a separate load case (see Section 2.3), this example shows why it is meaningful. The shear stresses from the shear force has an important effect on elastic buckling. Investigating the separate effect of shear force is nearly impossible with commercial FEM, since a pure V case is hard to define, and/or it is hard to switch on/off the effect of shear. In general, while ignoring the effect of shear force can be justified in many practical situations, in the buckling of tubular members the impact of shear force seems to be important (consistent with [25]).

3.6 Nonuniform geometry, nonuniform loading

To illustrate the ability of the developed method to handle step-wise (slightly) tapered tubes, two further examples are considered.

In the Cantilever #3 example, see Fig. 14, the member length is 500 mm, and the radius decreases from 100 mm (at the clamped end) to 96 mm (at the free end). Five pieces of equal-length segments are considered, hence the radii are 100, 99, 98, 97, and 96 mm. The thickness varies, too: it is 1 mm at the clamped end, and then increases to 1.2 mm, 1.4 mm, 1.6 mm and 1.8 mm. The material is steel (as before). The support conditions are an ideal cantilever, same as in cantilever example #1. The loading is an upward concentrated force F at the cantilever free end, acting at an eccentricity, e. Three values for the eccentricity are considered here e= 25 mm, 500 mm, and 2500 mm; leading to ratios of torque to the maximum bending moment of 0.05, 1, and 5, respectively. Practically, therefore, when T/M=0.05, the loading is primarily bending (plus shear), while in the case of T/M=5 torsion dominates.

The shell FEM model is similar to that in Cantilever #1. Moreover, the eccentric concentrated force is imposed as follows: first, it is substituted by a concentric force and an end torque; then, both the upward force and the torque are imposed as equivalent edge loads following the proper shear flow distributions (i.e., in the case of a torque the shear flow is constant, in the case of a vertical force the shear flow is sinusoidal). Again, the reason is to avoid the localized effects and hoop stresses, which are not handled in the FTM. Moreover, the connections between the different diameter segments are realized by defining TIE type connections between the connecting cross-sections.

The critical load factors and the buckling shapes for shell FEM and FTM are provided in Fig. 15.

Note while the distribution of V and T is globally uniform and the distribution of M is globally linear, the stresses considered in FTM are uniform and linear only within the segments, while there are (small) jumps in the stress values across segments as the cross-sections change.

The observed buckling behavior is strongly affected by the T/M ratio. Even if the T/M ratio is very small and the buckling lobes are concentrated at the most compressed part of the member, the lobes are still inclined due to the torsion. When T/M=1, the buckling is governed by the shear stresses from T and V, but the inclined buckling lobes are somewhat shifted toward the top part of the cantilever due to the compressive stresses from M. Even though V and T are constant along the length, the intensity and inclination of the buckling lobes vary, partly due to the varying normal stresses, but also due to the effect of geometry changes along the length. Finally, if T/M is large, the buckling is dominated by the torque, though the buckled shape is not totally point-symmetric due to the presence of V and M.

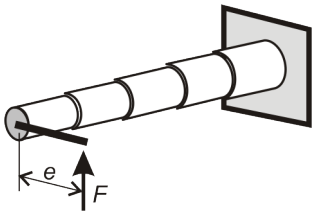

Figure 14: Arrangement for Cantilever #3

	T/M=0.05, e=25 mm	T/M=1, e=500 mm	T/M=5, e =2500 mm
Abaqus	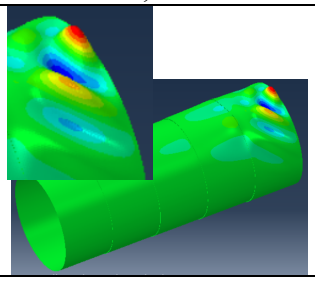	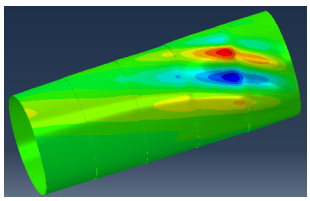	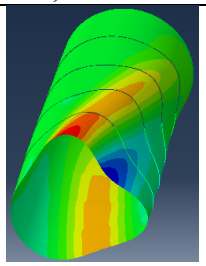
shell FEM	lf_{cr}=80.387 DOF=489840	lf_{cr}=35.419 DOF=489840	lf_{cr}=8.9910 DOF=489840

FTM	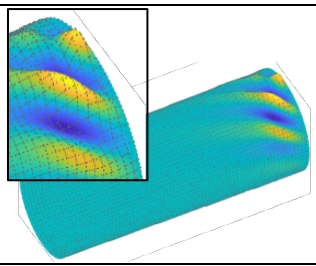	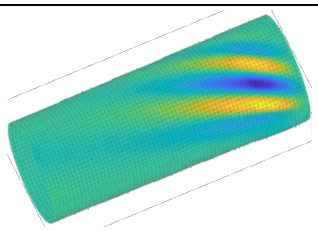	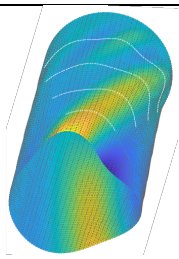
	lf_{cr}=79.846 q=9, DOF=4785	lf_{cr}=34.289 q=9, DOF=4785	lf_{cr}=9.2284 q=9, DOF=4785

Figure 15: Cantilever #3, buckled shapes, critical load factors

The agreement between FTM and shell FEM is not perfect (+/-3% in lf_{cr}), but reasonably good, for both critical loads and buckled shapes, though FTM uses fewer DOF compared to shell FEM. The primary reason for the differences is in the stress distribution: in the case of FTM the stresses are idealized (i.e., the longitudinal distribution is perfectly uniform or linear within each segment), while in the case of shell FEM the stresses are disturbed at the locations of radius/thickness changes. (Moreover, in the case of FTM the hoop stresses are disregarded, while in the shell FEM they are considered, even though they are small.) While the 1 mm step in the radius might seem small, it is in the range of the thickness; hence, it is significant compared to the radius changes in real wind turbine towers. Despite the significant radius change, approximation of internal stresses, and ignoring hoop stress the FTM solution is more than adequate.

Example Cantilever #4 is the quasi-tapered version of Cantilever #2. The radius remains 125 mm at the clamped end, but gradually decreases to 100 mm. Within the 750 mm total tube length 5 pieces of 150-mm-long segments are applied. All the other parameters are identical to those in Cantilever #2. Fig. 16 summarizes the results.

Observations for the tapered case (#4) are essentially identical to those for the non-tapered case (#2). However, there are some further noteworthy observations regarding the effect of tapering. The slight tapering has a small influence on the buckled shapes and a negative effect in general, as the critical force values are reduced compared to the non-tapered case. (Note, the total amount of material in the tapered case is reduced, too.) The amount of critical force reduction is dependent on the loading. Considering pure load cases, in the case of M, the critical force reduction from tapering is practically zero. For M alone, the buckling is localized at the clamped end, primarily in the first prismatic segment which has the same R and t as the untapered case. In the case of isolated N or V there is only slight reduction in the critical force due to tapering; approximately 1-1.5%. The largest influence of tapering is experienced in the case of T, where the reduction is 12%. In the combined loading cases the reduction is basically determined by the load components. Whenever T is included, the reduction is relatively significant, around 10%. If T is not involved, the reduction is small, not greater than 1%.

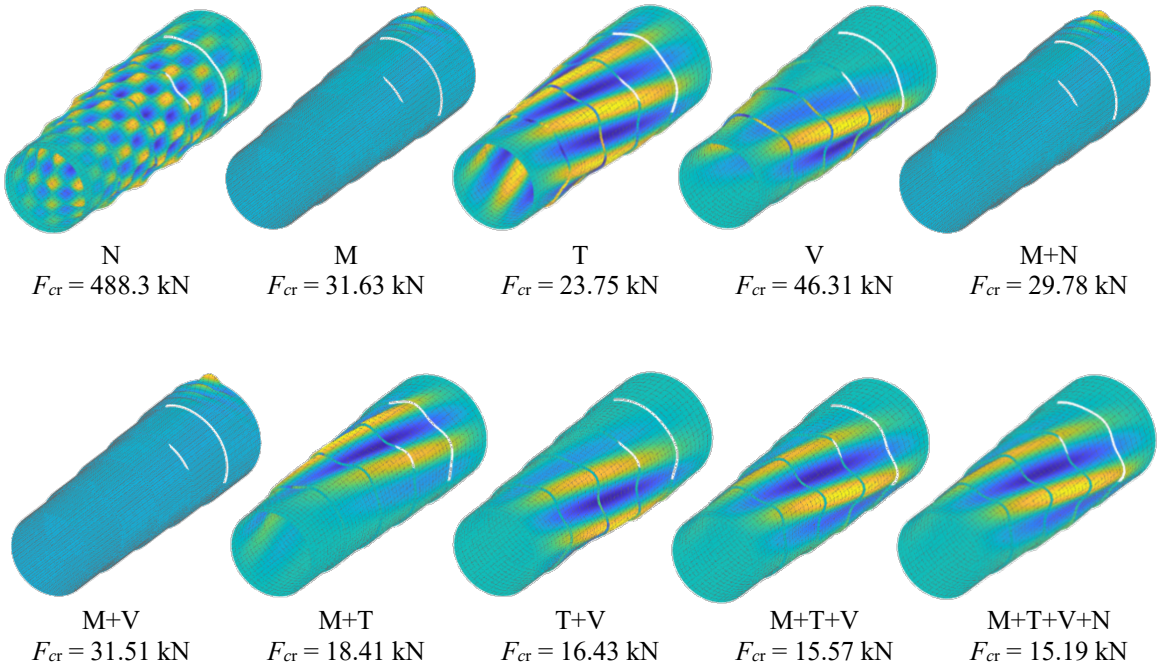

Figure 16: Tapered cantilever, R=125-100, t=0.79, L=750, T/M=1/3

4. Discussion

In developing FTM a number of options are possible. Here we provide more in-depth discussions on the kinematics selected and the ramifications, as well as the longitudinal shape functions (Fourier series) considered. Finally, we also provide discussion on future developments for FTM and its intended application.

4.1 The effect of modifications in strain calculation

As mentioned is Section 2.2, in the definition of the strain components Sanders' work is followed (as given in [9,16,20]), but with some differences.

Nonlinear longitudinal normal strain

One difference is how the nonlinear part of the longitudinal strain is calculated. In [9] and [16] the following formula is employed:

$$\varepsilon_y{}^{NL} = \frac{1}{2}\left(\beta_x{}^2 + \beta_z{}^2\right) \tag{41}$$

This formula is the one typically employed when beam theory is followed, i.e., when the buckling of beam-like structural members is investigated. In plate-theory-based analysis of thin-walled members, however, it is more typical to calculate this strain component with an additional term, see e.g., the semi-analytical FSM, Chung, CUFSM software, cFEM, or any shell FEM solution [17,18,21]. In this case the formula is as follows.

$$\varepsilon_y{}^{NL} = \frac{1}{2}\left(\beta_x{}^2 + \left(\frac{\partial v}{\partial y}\right)^2 + \beta_z{}^2\right) \tag{42}$$

The practical experience is that the additional strain term has little influence in linear buckling analyses [16], still, it is fair to say that out of the two versions it is Eq. (42) which is the more

precise representation of the displacement-stress relationship. Furthermore, FTM is intended to be applicable for a wide range of problems, including short members, to which the plate/shell theory fits better. Therefore, in FTM Eq. (42) is employed, see also. Eq. (5).

The $(\partial v/\partial y)^2$ term is part of ${\varepsilon_y}^{NL}$, which is the strain work compatible with σ_y. Consequently, $(\partial v/\partial y)^2$ has effect only if longitudinal normal stresses are present, e.g., if the load is N and/or M. We have analyzed this effect numerically, and we concluded that the caused difference is always small. In a more detailed way, focusing on the first buckling modes, the following conclusions have been drawn: (i) considering $(\partial v/\partial y)^2$ decreases the critical load; (ii) the maximum difference is less than 1%, which occurs in the case of shell-type buckling under the effect of N (i.e., medium length columns), but in any other case the difference is less than 0.1%.; (iii) for lengths where global (flexural or lateral-torsional) buckling governs, the difference is even smaller, and converges to zero as the length keeps increasing. So, the $(\partial v/\partial y)^2$ effect can always be regarded practically negligible. Its consideration is optional, but if considered, the theory is mechanically more consistent with the theory behind FSM or shell FEM.

Drilling rotation

Another difference is the definition of β_z, in Eq. (2), which can be understood as the drilling rotation. In [9] and [16] it is calculated as

$$\beta_z = \frac{1}{2}\left(-\frac{\partial u}{\partial y} + \frac{\partial v}{\partial x}\right) \tag{43}$$

while in the here-introduced FTM it is calculated as:

$$\beta_z = -\frac{\partial u}{\partial y} \tag{44}$$

It is clear from the formulae, that this modification has effect on both the elastic and geometric stiffness matrices, in any load case. As the results prove, occasionally it has a large effect. This is illustrated in Fig. 17 for an isotropic steel tube with *R*=50mm, *t*=1mm, and loading as shown.

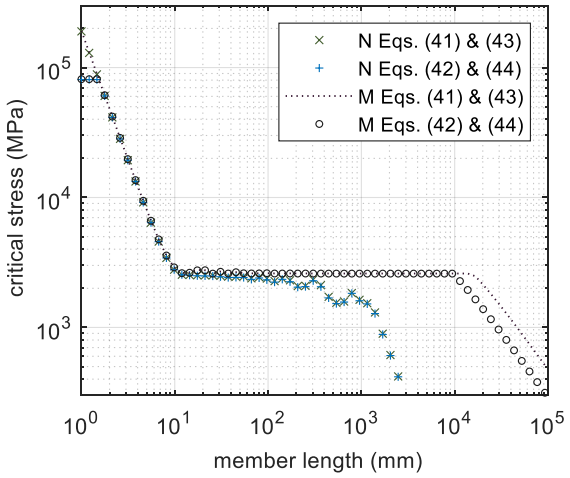

Figure 17: The effect of β_z calculation (R=50mm, t=1mm)

From the numerical results the following observations are worth mentioning. (i) When the length is very short (smaller than half of L_c, L_c being the half-wavelength where the minimum of

axisymmetric mode occurs), the difference caused by the calculation of β_z can be large, and it increases as the length decreases. Obviously, these lengths are extremely small ones, therefore, even though the β_z effect is numerically significant, it has little or no practical importance. (ii) For medium length members subjected to N, i.e., in the length range where the buckling is shell-shaped, the difference is around 1%, with a maximum of 2%. The difference is smaller in any other load case. (iii) In the case of N, T or V, the difference becomes smaller as the governing buckling becomes global; and the difference converges to zero as the length increases. (iv) In the case of M, β_z causes a significant difference when global (LT) mode governs. The original Sanders' proposal gives approx. 37-39% higher critical values compared to the ones calculated with the modified β_z. (Note, these latter results well coincide with the analytical results; in fact, if the member is long enough, the agreement is nearly perfect, see Table 2.)

As far as this (surprisingly) big influence of β_z on LT buckling is concerned, in the original Sanders' proposal a general shell surface was assumed, without any characteristic directions. However, in the case of a thin-walled member, there always are the longitudinal and transverse directions, naturally defined by the member geometry. In Sanders' proposal the drilling rotation (i.e., β_z) of an elementary surface area is calculated as the average of the inclinations of the two perpendicular sides of the elementary area (i.e., average of $-\partial u/\partial y$ and $\partial v/\partial x$). In the analysis of beam-like members; however, the inclination of a longitudinal fiber is always associated with (and only with) the transverse translational displacements (i.e., u and/or w), and never associated with the longitudinal translations (i.e., v, which are called warping displacements in thin-walled beam theories). These terms are included in the nonlinear longitudinal strain ${\varepsilon_y}^{NL}$, which has important role in calculating the work (external potential) if the load involves longitudinal normal stress σ_y.The difference between Eq. (43) and Eq. (44) becomes significant if v is (nearly) zero, but u is important. This is the case when the deformation of the tube involves rigid-body twist, which happens, e.g., in LT buckling: even if the twisting rotation is small, LT buckling is not possible without it. β_z by Sanders' way is half of the β_z by the modified formula if $v = 0$. This difference is directly transmitted to the work, and will result in a 1 to 2 ratio in the torsional rigidity, which finally leads to a 1 to $\sqrt{2}$ ratio in the critical load. The numerical experience is (see e.g. the example shown in Fig. 17) that this ratio is 1.37-1.39, and increasing with the length, i.e., it is getting closer to $\sqrt{2}$. The small difference between the analytical prediction and the numerical result is due to the fact that v and w are not precisely zero.

It would be unfair to say that either the Sanders' way or the modified way for the calculation of β_z is 'good' or 'wrong'. If the analyzed surface is a generic shell surface, Sanders' definition of the drilling rotation is reasonable. However, if the shell structure is so specific as a (very) long tubular member, it is more reasonable to adopt the modified way. As the numerical results show, both ways lead to similar results for normal-length tubes; hence, both ways can be judged as practically applicable for a wide length range. However, if the method is to be applied for extremely long members, it seems more appropriate to use the modified formula for the calculation of β_z.

Nonlinear membrane shear strain

In [9] and [16] the nonlinear membrane shear strain is calculated as

$$ {\gamma_{xy}}^{NL} = \beta_x \beta_y \tag{45} $$

where β_x and β_y can be understood as the slopes of the deformed surface (i.e., rotation around the x and y axis, respectively), essentially due to the out-of-surface (i.e., w) displacements. In the here-introduced FTM it is calculated as:

$$\gamma_{xy}{}^{NL} = \left(\frac{\partial u}{\partial x} + \frac{w}{R}\right)\frac{\partial u}{\partial y} + \frac{\partial v}{\partial x}\frac{\partial v}{\partial y} + \beta_x\beta_y \tag{46}$$

The considered extra two terms represent (essentially) the effect of the membrane displacements. It is clear that this modification has effect only when shear stresses are present, i.e., when the stress comes from torque and/or shear force. The practical effect is illustrated in Fig. 18.

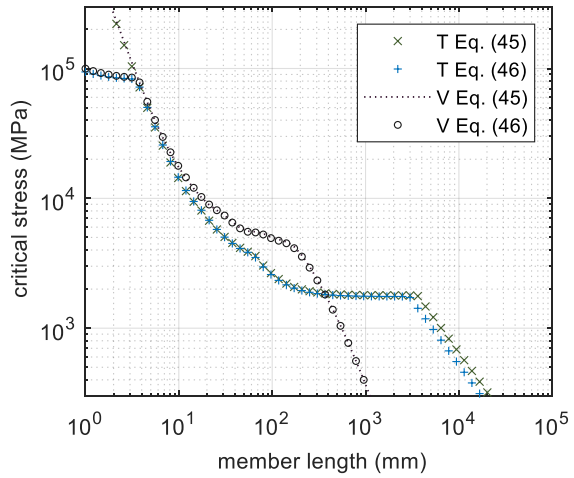

Figure 18: The effect of nonlinear shear strain formulae (R=10mm, t=1mm)

The observations are as follows. (i) When the length is very short (i.e., smaller than L_c), the difference caused by the calculation of $\gamma_{xy}{}^{NL}$ can be large, and it increases as the length decreases. With Eq. (45) the critical load seems to tend to infinity, while with Eq. (46) it seems to tend to a finite value as the member length approaches zero. These lengths are very small, the difference caused has little or no practical importance. (ii) For medium length members the difference caused by the calculation of $\gamma_{xy}{}^{NL}$ remains fairly small. The difference increases with the decreasing of the R/t ratio: in the considered cases the maximum difference is 2-3% when R/t =10; for the investigated larger R/t ratios the differences are below 1%. (iii) When the member is long enough to experience global buckling, the effect of $\gamma_{xy}{}^{NL}$ is dependent on the loading. In the case of V loading the effect is negligible. However, in the case of T loading the effect is important, as well visible in Fig. 18, too. Applying the simplified formula for $\gamma_{xy}{}^{NL}$ increases the critical torque value, by approx. 22%. As a conclusion, both the more precise Eq. (46) and the simpler Eq. (45) can be judged as practically applicable for a wide length range. However, if the method is to be applied for very short or very long members, it seems more appropriate to use the more precise formula. This observation is in full agreement with the conclusion of [26], which was drawn from the analysis of the helical buckling of long tubes with regular polygonal cross-sections.

4.2 The effect of longitudinal shape functions

As mentioned in Section 2.1, and detailed in Appendix A, two versions of the longitudinal shape functions are implemented: sin-cos and sin-only. Implications of these choices on accuracy and efficiency are briefly addressed in the following.

sin-cos version

In simple, very regular cases a very small number of terms can be enough. E.g., in the case of pure compression, with pinned supports, even a single longitudinal term can lead to exact results. If the case is not totally regular, multiple terms are necessary. In the authors experience, increasing the number of terms can cause numerical instability, even when the number of terms is not very high. As a rule of thumb, more than 20 terms may cause problems. A potential solution to the numerical issue is to utilize multiple segments along the tube length. This is possible and it helps; however, if segmentation is applied, several terms must be considered within each segment. Consider e.g., global buckling of a longer member. The buckled shape is a single halfwave, but if multiple segments are applied the shape of a single segment is almost a rigid-body rotation, which requires several trigonometric terms to approximate and therefore, applying a relatively large number of segments (with several terms in each segment) is a possible solution, but in this case the computational efficiency of the method is partly lost.

sin-only version

If the cosine terms are eliminated, the issues of the sin-cos version are eliminated. Even with a few hundred terms no numerical instability is experienced. The consequence is that segmentation is not necessary, unless the problem to be analyzed makes it necessary (e.g., the member has quasi-tapered geometry). The disadvantage is that some classic cases cannot be analyzed with a small number of terms. Consider a compressed pin-ended tube. The out-of-plane translations are sinusoidal, while the longitudinal translation is (should be) cosine. Since in the displacement approximation the cosine terms are missing, the cosine terms must be approximated by the sine terms and the linear term that we augment the sine series with. From practical experience (as a rule of thumb) a minimum of 7 sine terms are necessary. This is still a small number of degrees of freedom; moreover, even in the sin-cos approach the cases where only extremely small number of terms are applicable is limited. Therefore, this “disadvantage” of the sin-only approach means hardly any practical disadvantage in a generic case. Another experience is that if the ends of the member are clamped, the lack of cos terms means that more sin terms are necessary.

4.3 Further features of the FTM

With the developed method spectral analysis of the results can readily be performed since the solution is obtained in the form of Fourier series. This feature is implemented, though not discussed in this paper. Moreover, the implemented spectral analysis can be utilized for any displacement field, e.g., for measured geometric imperfections of real tubular members.

The method herein was also supplemented by a tool to determine the shape of the buckling lobes. From the shape, the characteristic buckling lengths in any direction can be calculated. The notion of ‘buckling length’ is classical, widely used in buckling analysis of columns, beams, and frames, but hardly applied to shell buckling. The developed tool makes it possible to discuss the shell buckling problem from the aspect of buckling length.

Finally, model identification and decomposition options have also implemented with FTM, allowing the notions of local, distortional, and global buckling modes of thin-walled members to be extended to thin-walled tubes.

These features and a code repository so users may utilize FTM all are under development and will be the subject of future publications from the authors.

5. Conclusions

In this paper a numerical method for the linear buckling analysis of cylindrical tubes was introduced. The method can handle tubular members built up from prismatic cylindrical segments. Any combination of axial, shear, moment, and torsion loading is allowed, however, it is assumed that the stress distribution is smooth (i.e., there are no localized stress concentrations). Small geometric changes (radius and/or thickness) between the adjoining segments along the length are allowed, making it possible to analyze quasi-tapered tubular structures, as typical for the supporting towers of wind turbines. Since the building block of the method is a tubular segment, the method is termed the Finite Tube Method, abbreviated as FTM.

In the kinematic equations of FTM the curved nature of the tubular surface is directly considered. This, together with the applied Fourier series displacement approximation, makes the method numerically efficient, utilizing fewer degrees of freedom of a comparable shell finite element elastic buckling solution. Moreover, the importance of identified nonlinear strain terms was highlighted, which were found to be necessary in the case of extreme geometries.

In the paper FTM was validated against a large series of numerical calculations: varying length, radius, thickness, and loading (axial, shear, moment, and torsion) including combined loading and also demonstrating cases with longitudinal stress gradients and step-wise longitudinal geometric changes. In general, it was shown that elastic buckling via FTM is efficient and applicable in an extremely wide range of parameters. In simple cases, where (reasonably exact) analytical solutions exist, the FTM results match well. FTM is much more general than existing analytical solutions, and unique but practical problems for the stability of tubes under combined loading are provided and discussed. In more general cases the FTM results were compared to those from shell finite element calculations. Very good agreement was found for cases when the stress states considered in FTM and calculated by shell finite elements are similar. It is noted that when the stress state is complex, and/or when the stress state is locally affected by abrupt and significant geometric changes, additional enhancements to the FTM's calculation of internal stresses may be warranted.

The authors are still actively developing FTM and extensions planned in the future include considering hoop stresses, and adding the option to calculate internal stresses by a linear static analysis. Already the authors have utilized FTM's framework for examining spectral representations of buckling shapes, for uniquely defining buckling length in shells, and have recently implemented a force-based constraint method that enables modal identification and modal decomposition techniques currently used in other thin-walled members. These works are the subject of forthcoming papers from the authors.

Acknowledgments

This material is based upon work supported by the National Science Foundation under Grant No. 1912481 and No. 1912354. Any opinions, findings, and conclusions or recommendations

expressed in this material are those of the authors and do not necessarily reflect the views of the National Science Foundation.

References

1. CEN, EN 1993-1-6:2021, Eurocode 3, Design of Steel Structures, Part 1-6: Strength and Stability of Shell Structures. (2021)
2. Koiter, W. T., The Stability of Elastic Equilibrium, TU-Delt. English Translation by E. Riks, provided by U.S. Air Force Flight Dynamics Laboratory. (1945)
3. Donnell, L. H., Stability of Thin-Walled Tubes Under Torsion, National Advisory Committee for Aeronautics. Report No. 479. (1933)
4. Timoshenko, S.P., Gere, J. M., Theory of Elastic Stability, McGraw Hill (reprinted by Dover in 2009), p 541. (1961)
5. Flügge, W., Stresses in Shells, Springer-Verlag, p 499. (1962)
6. Mahmoud, A., Torabian, S., Jay, A., Mirzaie, F., Myers, A. T., Smith, E., Schafer, B.W., Modeling the flexural collapse of thin-walled spirally welded tapered tubes, *Journal of Structural Engineering,* Vol. 144(2): 04017201, p 14. (2018)
7. Sadowski, A.J., On the advantages of hybrid beam-shell structural finite element models for the efficient analysis of metal wind turbine support towers, *Finite Elements in Analysis and Design*, Vol. 162. pp. 19-33. (2019)
8. Filippidis, A., Sadowski A.J., Modern analysis of axisymmetric shells with AQUINAS: A MATLAB finite element toolbox., *SoftwareX*, 23, 101434. (2023)
9. Silvestre N., Generalised beam theory to analyse the buckling behaviour of circular cylindrical shells and tubes, *Thin-Walled Structures*, Vol 45, pp. 185-198. (2007)
10. Basaglia, C., Camotim, D., Silvestre, N., Buckling and vibration analysis of cold-formed steel CHS members and frames using Generalized Beam Theory, *Int. J. Struct. Stab. Dyn*., 15 (08), 1540021. (2015)
11. Basaglia, C., Camotim, D., Silvestre, N., GBT-Based buckling analysis of steel cylindrical shells under combinations of compression and external pressure, *Thin-Walled Struct.,* Vol 144, 106274. (2019)
12. Muresan, A-A., Nedelcu, M., Gonçalves, R., GBT-Based FE formulation to analyse the buckling behaviour of isotropic conical shells with circular cross-section, *Thin-Walled Struct*., Vol 134, pp 84–101 (2019)
13. Habtemariam, A.K., Könke, C., Zabel, V., Bianco, M.J., Generalized Beam Theory Formulation for thin-walled pipes with circular axis, *Thin-Walled Struct.*, Vol 159, 107243. (2021)
14. Habtemariam, A.K., Bianco, M.J., Könke, C., Zabel, V., Geometrically nonlinear formulation of Generalized Beam Theory for the analysis of thin-walled circular pipes, *Thin-Walled Structures*, Vol 173, 109029. (2022)
15. Nedelcu, M., New unified family of GBT deformation modes for the analysis of thin-walled cylinders, *Thin-Walled Structures*, Vol 183, 110334. (2023)
16. Nedelcu, M., First-order and linear buckling analysis of thin-walled cylinders using new GBT deformation modes, *Thin-Walled Structures*, Vol 189, 110950. (2023)
17. Cheung, Y.K., Tham, L.G., *Finite Strip Method*, CRC Press. (1997)
18. Schafer B.W., Ádány S., Buckling analysis of cold-formed steel members using CUFSM: conventional and constrained finite strip methods. Proceedings of 18th International

specialty conference on cold-formed steel structures, Orlando, USA, October 26–28, 2006. pp.39–54. (2006)
19. Ding, V., Abdelrahman, A.H.A., Lin, D., Shields, M.D., Myers, A.T., Krabbe, M., Schafer B.W., Classical and Finite Element Methods for Elastic Buckling of Cylindrical Shells. *Proceedings* of the Annual Stability Conference, Structural Stability Research Council, Louisville, Kentucky, USA, April 14-15, 2021. p 20. (2021)
20. Sanders, J.L., Non-linear theories for thin shells, Quarterly of Applied Mathematics, Vol 21(1), pp. 21–36. (1963)
21. Ádány S., Visy D., Global Buckling of Thin-Walled Columns: Numerical Studies, *Thin-Walled Structures*, Vol 54, pp 82-93. (2012)
22. Pham C.H., Hancock G.J., Shear buckling of thin-walled channel sections, *Journal of Constructional Steel Research*, 65 (3), pp. 578-585. (2009)
23. Dessault Systems Simulia Corp., Abaqus Software. (2022)
24. Victoria Ding, V., Torabian, S., Adany, S., Yun, X., Pervizaj, A., Myers, A.T., Schafer, B.W., Experimental Results on Stability of Cylindrical Shells Under Combined Bending and Torsion, *Journal of Structural Engineering*, in press. (2024)
25. Schmidt H., Winterstetter Th.A., Cylindrical shells under torsional and transverse shear, In: *Buckling of Thin Metal Shells* (eds: Rotter T.M., Teng J.G.), Spon Press, London, pp. 207-229. (2004)
26. Rendall, M.A., Hancock, G.J. and Rasmussen, K.J., Modal buckling behaviour of long polygonal tubes in uniform torsion using the generalised cFSM, *Thin-Walled Structures*, Vol. 128, pp.141-151. (2018)
27. Seide, P., Weingarten, V.I., On the Buckling of Circular Cylindrical Shells Under Pure Bending. *Transactions of the ASME*, pp. 112-116. (1961)
28. Greenhill A., On the strength of shafting when exposed both to torsion and to end thrust, *Proc. Inst. Mech. Eng*. pp. 182–228. (1883)

APPENDICES

Appendix A: Approximation of the displacements

The displacement functions are approximated identically, by full Fourier series. Thus, any *d* displacement is approximated as:

$$d(x,y) = d_x(x) \cdot d_y(y) \tag{A1}$$

In the circumferential direction full Fourier-series approximation is used, with even number of half-waves:

$$d_x(x) = a_0 + \sum_{i=1}^{p} \left(a_{s,i}\, sin\frac{ix}{R} + a_{c,j}\, cos\frac{ix}{R} \right) \tag{A2}$$

In the longitudinal direction, Fourier-like approximation is used, but in two versions. One version uses full Fourier-series:

$$d_y(y) = b_0 + \sum_{j=1}^{q} \left(b_{s,j} sin\frac{j\pi y}{l} + b_{c,j}\, cos\frac{j\pi y}{l} \right) \tag{A3a}$$

The other version uses a constant term, a linear term, and only the sine terms:

$$d_y(y) = b_0 + b_1 \frac{y}{l} + \sum_{j=1}^{q} \left(b_{s,j} sin\frac{j\pi y}{l} \right) \tag{A3b}$$

Substituting Eq (2) and Eq (3a) into Eq (1) leads to:

$$d(x,y) = \left[a_0 + \sum_{i=1}^{p} \left(a_{s,i}\, sin\frac{ix}{R} + a_{c,j}\, cos\frac{ix}{R} \right) \right] \cdot \left[b_0 + \sum_{j=1}^{q} \left(b_{s,j} sin\frac{j\pi y}{l} + b_{c,j}\, cos\frac{j\pi y}{l} \right) \right] \tag{A4}$$

Therefore:

$$\begin{aligned} d(x,y) = {} & a_0 b_0 + \sum_{i=1}^{p} \left(a_{s,i}\, b_0 sin\frac{ix}{R} \right) + \sum_{i=1}^{p} \left(a_{c,i}\, b_0 cos\frac{ix}{R} \right) + \\ & \sum_{j=1}^{q} \left(a_0 b_{s,j} sin\frac{j\pi y}{l} \right) + \sum_{j=1}^{q} \left(a_0 b_{c,j} cos\frac{j\pi y}{l} \right) + \sum_{i=1}^{p} \sum_{j=1}^{q} \left(a_{s,i} b_{s,j}\, sin\frac{ix}{R} sin\frac{j\pi y}{l} \right) + \\ & \sum_{i=1}^{p} \sum_{j=1}^{q} \left(a_{c,i} b_{s,j}\, cos\frac{ix}{R} sin\frac{j\pi y}{l} \right) + \sum_{i=1}^{p} \sum_{j=1}^{q} \left(a_{s,i} b_{c,j}\, sin\frac{ix}{R} cos\frac{j\pi y}{l} \right) + \\ & \sum_{i=1}^{p} \sum_{j=1}^{q} \left(a_{c,i} b_{c,j}\, cos\frac{ix}{R} cos\frac{j\pi y}{l} \right) \end{aligned} \tag{A5}$$

The product of a and b coefficients can readily be replaced by new, say, *d* coefficients:

$$\begin{aligned} d(x,y) = {} & d_{00} + \sum_{i=1}^{p} \left(d_{s0,i}\, sin\frac{ix}{R} \right) + \sum_{i=1}^{p} \left(d_{c0,i}\, cos\frac{ix}{R} \right) + \\ & \sum_{j=1}^{q} \left(d_{0s,j} sin\frac{j\pi y}{l} \right) + \sum_{j=1}^{q} \left(d_{0c,j} cos\frac{j\pi y}{l} \right) + \sum_{ij=1}^{p\times q} \left(d_{ss,ij}\, sin\frac{ix}{R} sin\frac{j\pi y}{l} \right) + \\ & \sum_{ij=1}^{p\times q} \left(d_{cs,ij}\, cos\frac{ix}{R} sin\frac{j\pi y}{l} \right) + \sum_{ij=1}^{p\times q} \left(d_{sc,ij}\, sin\frac{ix}{R} cos\frac{j\pi y}{l} \right) + \sum_{ij=1}^{p\times q} \left(d_{cc,ij}\, cos\frac{ix}{R} cos\frac{j\pi y}{l} \right) \end{aligned} \tag{A6}$$

To be more general, $d(x,y)$ can be expressed as follows:

$$\begin{aligned} d(x,y) = {} & d_{00} f^{00} + \sum_{i=1}^{p} d_{s0,i} f^{s0} + \sum_{i=1}^{p} d_{c0,i} f^{c0} + \\ & \sum_{j=1}^{q} d_{0s,j} f^{0s} + \sum_{j=1}^{q} d_{0c,j} f^{0c} + \sum_{ij=1}^{p\times q} d_{ss,ij} f^{ss} + \sum_{ij=1}^{p\times q} d_{cs,ij} f^{cs} + \sum_{ij=1}^{p\times q} d_{sc,ij} f^{sc} + \\ & \sum_{ij=1}^{p\times q} d_{cc,ij} f^{cc} \end{aligned} \tag{A7}$$

The above steps can be performed similarly in the other version, and the final expression for $d(x,y)$ takes the same format, however, with (partly) different *f* functions. The *f* functions are summarized in Fig. A1.

number of terms	version 'sin-cos'	version 'sin-only'
1	$f^{00}(x,y) = (1)(1)$	$f^{00}(x,y) = (1)(1)$
p	$f^{s0}(x,y) = \left(sin\frac{ix}{R}\right)(1)$	$f^{s0}(x,y) = \left(sin\frac{ix}{R}\right)(1)$
p	$f^{c0}(x,y) = \left(cos\frac{ix}{R}\right)(1)$	$f^{c0}(x,y) = \left(cos\frac{ix}{R}\right)(1)$
q	$f^{0s}(x,y) = (1)\left(sin\frac{j\pi y}{l}\right)$	$f^{0s}(x,y) = (1)\left(sin\frac{j\pi y}{l}\right)$
$p \times q$	$f^{ss}(x,y) = \left(sin\frac{ix}{R}\right)\left(sin\frac{j\pi y}{l}\right)$	$f^{ss}(x,y) = \left(sin\frac{ix}{R}\right)\left(sin\frac{j\pi y}{l}\right)$
$p \times q$	$f^{cs}(x,y) = \left(cos\frac{ix}{R}\right)\left(sin\frac{j\pi y}{l}\right)$	$f^{cs}(x,y) = \left(cos\frac{ix}{R}\right)\left(sin\frac{j\pi y}{l}\right)$
q or 1	$f^{0c}(x,y) = (1)\left(cos\frac{j\pi y}{l}\right)$	$f^{01}(x,y) = (1)\left(\frac{y}{l}\right)$
$p \times q$ or p	$f^{sc}(x,y) = \left(sin\frac{ix}{R}\right)\left(cos\frac{j\pi y}{l}\right)$	$f^{s1}(x,y) = \left(sin\frac{ix}{R}\right)\left(\frac{y}{l}\right)$
$p \times q$ or p	$f^{cc}(x,y) = \left(cos\frac{ix}{R}\right)\left(cos\frac{j\pi y}{l}\right)$	$f^{c1}(x,y) = \left(cos\frac{ix}{R}\right)\left(\frac{y}{l}\right)$

Figure A1: Fourier terms for the displacement functions.

Eq. (A7) can be expressed in a more compact form, slightly symbolically, as:

$$d(x,y) = \sum_{k=1}^{n} d_k f_k \tag{A8}$$

where n is the total number of terms, determined by the number of terms in the circumferential and meridian directions (p and q, respectively). In version 'sin-cos':

$$n = (2p+1)(2q+1) \tag{A9a}$$

In version 'sin-only':

$$n = (2p+1)(q+2) \tag{A9b}$$

Accordingly, any of the u, v, and w translations are expressed similarly, as:

$$u(x,y) = \sum_{k=1}^{n} u_k f_k(x,y) \quad v(x,y) = \sum_{k=1}^{n} v_k f_k(x,y) \quad w(x,y) = \sum_{k=1}^{n} w_k f_k(x,y) \tag{A10}$$

Appendix B: Pure loading cases

In the circumferential direction the stress is assumed to be either constant or sinusoidal. Based on the circumferential distribution, therefore, 6 basic loading situations can be considered: pure N, pure M_X, pure M_Z, pure T, pure V_X, and pure V_Z as illustrated in Fig. B1.

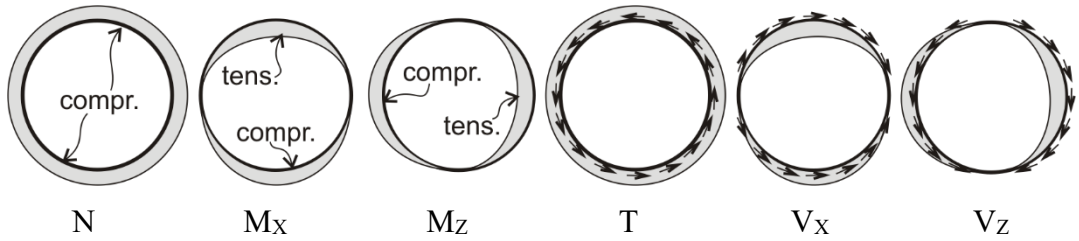

Figure B1: Stress distributions (along the cross-section midline) for pure loading cases

The considered normal stress functions are given as follows:

$$\sigma_N(x,y) = \sigma_0 g(y) \tag{B1}$$

$$\sigma_{M,X}(x,y) = -\sigma_0 \, sin\frac{x}{R} g(y) \tag{B2}$$

$$\sigma_{M,Z}(x,y) = -\sigma_0 \, cos\frac{x}{R} g(y) \tag{B3}$$

where σ_0 is the maximum (compressive, positive) stress in the cross-section, and $g(y)$ is the function that describes the longitudinal distribution (which, in the implemented version, is up to a quadratic function). It can be understood that the using constant distribution along the circumference leads to a non-zero normal force (as stress resultant), and zero moments about any cross-section axes. Similarly, if the stress distribution is according to a sine or cosine function in the circumferential direction, it leads to zero normal force and non-zero moment about one axis, M_X or M_Z. The stress resultants are summarized in Fig. B2, where A is the cross-sectional area, R is the radius, and I_X and I_Z are the second moments of area for the X and Z axis, respectively (and in our case I_X=I_Z).

	$\int_0^{2\pi R} \sigma(x,y)\,dx$	$\int_0^{2\pi R} -Z\sigma(x,y)\,dx$	$\int_0^{2\pi R} -X\sigma(x,y)\,dx$
$\sigma_N(x,y)$	$N(y) = \sigma_0 A g(y)$	$M_X(y) = 0$	$M_Z(y) = 0$
$\sigma_{M,X}(x,y)$	$N(y) = 0$	$M_X(y) = \sigma_0 \frac{I_X}{R} g(y)$	$M_Z(y) = 0$
$\sigma_{M,Z}(x,y)$	$N(y) = 0$	$M_X(y) = 0$	$M_Z(y) = \sigma_0 \frac{I_Z}{R} g(y)$

Figure B2: Resultants from normal stresses.

Similarly, the considered shear stress functions are given as follows:

$$\tau_T(x,y) = \tau_0 g(y) \tag{B4}$$

$$\tau_{V,X}(x,y) = -\tau_0 \, sin\frac{x}{R} g(y) \tag{B5}$$

$$\tau_{V,Z}(x,y) = -\tau_0 \, cos\frac{x}{R} g(y) \tag{B6}$$

where τ_0 is the maximum shear stress in the cross-section. Fig. B3 summarizes the resultants from the shear stresses, which lead T torque, or to V_X or V_Z shear forces along the X and Z axis. It is to note that $\tau(x,y)\,cos\frac{x}{R}$ is the X-directional component of the actual shear force function, while $\tau(x,y)\,sin\frac{x}{R}$ is the Z-directional component of the shear force function. The involved cross-section

properties are as follows: I_0 is the polar moment of inertia, and A is the cross-sectional area, and it might worth mentioning that $A/2$ should be interpreted as the shear area along the *X* or *Z* axis.

	$\int_0^{2\pi R} R\tau(x,y)\,dx$	$\int_0^{2\pi R} -\tau(x,y)\,sin\frac{x}{R}dx$	$\int_0^{2\pi R} -\tau(x,y)\,cos\frac{x}{R}dx$
$\tau_T(x,y)$	$T(y)=\tau_0\frac{I_0}{R}g(y)$	$V_X(y)=0$	$V_Z(y)=0$
$\tau_{V,X}(x,y)$	$T(y)=0$	$V_X(y)=\tau_0\frac{A}{2}g(y)$	$V_Z(y)=0$
$\tau_{V,Z}(x,y)$	$T(y)=0$	$V_X(y)=0$	$V_Z(y)=\tau_0\frac{A}{2}g(y)$

Figure B3: Resultants from shear stresses.

Due to the symmetry of the circular tubes considered, it is rarely necessary to differentiate between M_X and M_Z, or between V_X and V_Z, i.e., the *X* and *Z* components of either the bending moment and the shear force can readily be combined into one – inclined – moment or shear. That is why it is enough to consider 'pure M' and 'pure V', i.e., practically 4 loading cases is distinguished.

Appendix C: Analytical buckling solutions for pure cases

C1. Pure N

For pure N, L mode, see e.g. [4]

$$\sigma_{cr}^{L}=\frac{E}{\sqrt{3(1-\nu^2)}}\frac{t}{R} \tag{C1}$$

For pure N, S modes, see e.g. [4], the minimum of

$$\sigma_{cr}^{S}=\frac{R_1 E}{S_1(1-\nu^2)} \tag{C2}$$

where

$$R_1=(1-\nu^2)\lambda^4+\alpha[(n^2+\lambda^2)^4-(2+\nu)(3-\nu)\lambda^4n^2+2\lambda^4(1-\nu^2)-\lambda^2n^4(7+\nu)+\lambda^2n^2(3+\nu)+n^4-2n^6]$$

$$S_1=\lambda^2\left\{(n^2+\lambda^2)^2+\frac{2}{1-\nu}\left(\lambda^2+\frac{1-\nu}{2}n^2\right)[1+\alpha(n^2+\lambda^2)^2]-\frac{2\nu^2\lambda^2}{1-\nu}+\frac{2\alpha}{1-\nu}\left(\lambda^2+\frac{1-\nu}{2}n^2\right)[n^2+(1-\nu)\lambda^2]\right\} \tag{C3}$$

where $\alpha=t^2/12R^2$ and $\lambda=m\pi R/L$, and m and n are positive integer numbers, being the assumed number of half-sine-waves along the tube length, and the number of full sine-waves along the circumference, respectively, and the minimum of σ_{cr}^{S} will belong to a particular *m,n* pair.

C2. Pure M

In the case of pure M, there is no exact solution for the L mode; typically, the same formula is used as for the axisymmetric mode to pure N, as an approximate solution, see Eq. (C1). It is to note that in [27] more exact solutions are given, but not in closed format.)

For pure M, LT mode, the classic formula is, considering that the warping is zero:

$$\sigma_{cr}^{LT} = \frac{\pi R}{L I_X}\sqrt{E I_z G I_0} \tag{C4}$$

where I_X is the moment of inertia, I_0 is the polar moment of inertia of the tubular section, and G is the shear modulus.

C3. Pure T

In the case of pure T, [3] gives an approximate solution as follows (for pinned-pinned supports). Whether S1 or S2 type buckling occurs is dependent on the J parameter, and the critical stress values are given as follows.

$$\begin{aligned} \tau_{cr}^{S1} &= \frac{AEt^2}{L^2(1-\nu^2)} \text{ if } J = \frac{L^2 t}{(2R)^3\sqrt{1-\nu^2}} < 5.5 \\ \tau_{cr}^{S2} &= \frac{BEt}{L\sqrt{1-\nu^2}} \text{ if } J = \frac{L^2 t}{(2R)^3\sqrt{1-\nu^2}} \geq 5.5 \end{aligned} \tag{C5}$$

with

$$A = 2.8 + \sqrt{2.6 + 1.40H^{1.5}} \text{ and } H = \frac{L^2}{2Rt}\sqrt{1-\nu^2} \tag{C6}$$

$$B = 0.77\sqrt{J} \tag{C7}$$

The formula for S2 buckling can be simplified as:

$$\tau_{cr}^{S2} = \frac{0.77E}{2\sqrt{2}(1-\nu^2)^{3/4}}\sqrt{\frac{t^3}{R^3}} \tag{C8}$$

Flügge [5] has a more exact formula for S2 type buckling, given as follows:

$$\tau_{cr}^{S2} = \frac{E}{3\sqrt{2}(1-\nu^2)^{3/4}}\sqrt{\frac{t^3}{R^3}} \tag{C9}$$

This formula is derived assuming infinitely long members, when the effect of end supports is negligible. For finite length tubes the solution is approximate. It is easy to notice that Donnell's and Flügge's solution are very similar, both are independent of the length, and Flügge's solution is approx. 15% smaller compared to Donnell's one.

Finally, for pure T, helical buckling, [28] presented an analytical solution as follows:

$$T_{cr}^{H} = \frac{E2I_X\pi}{L} \tag{C10}$$

from which the critical shear stress can be calculated as:

$$\tau_{cr}^{H} = \frac{T_{cr}^{H}}{I_0}R = \frac{E2I_X\pi R}{LI_0} = \frac{\pi ER}{L} \tag{C11}$$

C4. Pure V

There is no known analytical solution.